USING DIFFUSION TENSOR IMAGING TO ASSESS WHITE MATTER INTEGRITY IN CHILDREN WITH MATH DIFFICULITIES

By

Craig Thomas Lorang

Thesis

Submitted to the Faculty of the

Graduate School of Vanderbilt University

in partial fulfillment of the requirements

for the degree of

MASTER OF SCIENCE

in

Biomedical Engineering

December, 2007

Nashville, Tennessee

Approved:

Adam Anderson, Ph.D.

John Gore, Ph.D.

TABLE OF CONTENTS

LIST OF TABLES

LIST OF FIGURES

CHAPTER I

INTRODUCTION

Dyscalculia is a learning disability that affects up to 6% of all children (Geary 2004). This condition interferes with a person's ability to understand and manipulate numbers. There are several cognitive and performance features displayed by children with dyscalculia, which include:

1. Relatively frequent use of developmentally immature procedures
2. Frequent errors in the execution of procedures
3. Poor understanding of the concepts underlying procedural use
4. Difficulties sequencing the multiple steps in complex procedures
5. Difficulties retrieving mathematical facts, such as answers to simple arithmetic problems
6. For facts that are retrieved, there is a high error rate
7. For arithmetic, retrieval errors are often associates of numbers in the problem (e.g., retrieving 4 to 2 + 3 = ?; 4 is the counting-string associate that follows 2, 3)
8. Reaction times for correct retrieval are unsystematic
9. Difficulties in spatially representing numerical and other forms of mathematical information and relationships
10. Frequent misinterpretation or misunderstanding of spatially represented information

Dyscalculia can occur as a consequence of prematurity and low birthweight and is frequently encountered in a variety of neurological disorders, such as attention-deficit hyperactivity disorder (ADHD), developmental language disorder, epilepsy, and fragile X syndrome (Shalev 2004). Children with developmental dyscalculia benefit from early intervention, including programs that focus on basic numerical and conceptual knowledge (Kaufmann, Handl, and Thony 2003).

This study uses diffusion tensor imaging (DTI) to assess white matter integrity in children with math difficulties. The object is to determine if there is a structural difference in the white matter of children with math difficulties compared to children with normal math cognitive abilities.

Diffusion Tensor Imaging

Water Diffusion

Diffusion is a physical process that involves the translational movement of molecules via thermally driven random motions called Brownian motion. The mobility of the molecules can be characterized by a physical constant dubbed the diffusion coefficient, D, which is related to the root mean square displacement, RMS, of the molecules over a given time, t_{dif}, via the Einstein equation

$$RMS = \sqrt{2Dt_{dif}} \tag{1}$$

Several factors that influence diffusion in a solution are molecular weight, intermolecular interactions, and temperature (Beaulieu 2002) (Figure 1).

Figure 1. Brownian motion. Four identical particles begin at the origin, however each follows a different path due to thermal energy (collision with other molecules) (Beaulieu 2002).

The distance a molecule diffuses in one direction may or may not be the same as in another direction. In a pure liquid solution there are no obstructions or molecular hindrances, thus diffusion is equal in all directions. A physical property that is equal in all directions is termed isotropic, so diffusion is isotropic in this case. However, if diffusion is preferential by large in a certain direction, for example in a solution with oriented barriers, the diffusion is deemed anisotropic (Le Bihan et al. 2001) (Figure 2). This allows tissue subtypes to be identified simply by their diffusion characteristics, thus anisotropy is related to the underlying tissue geometry. The degree of hindrance to water diffusion is determined by size, shape, and composition of any physical boundary, as well as the distance between obstructions.

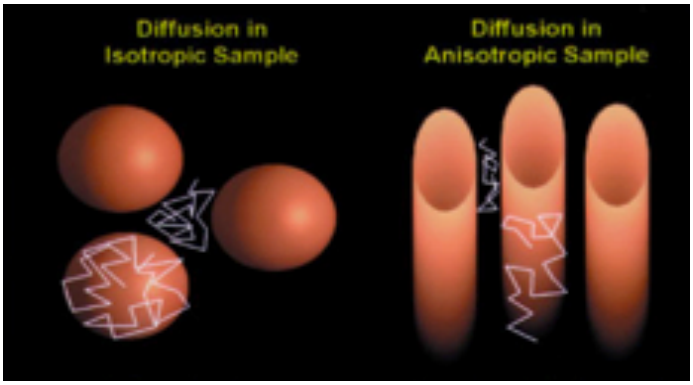

Figure 2. Isotropic and anisotropic diffusion. Molecules with equal diffusion in all directions experience isotropic diffusion. Molecules that that prefer diffusion in one direction to others experience anisotropic diffusion (Beaulieu 2002).

White matter tissue is highly anisotropic. This is mainly due to its specific organization into more or less myelinated axonal fibers running in parallel, however the underlying mechanisms are not fully understood. The myelin sheath around the axons, the axonal membrane, and the neurofibrils are all longitudinally oriented microstructures that are barriers to diffusion and reduce diffusion in the perpendicular direction with respect to parallel diffusion. DTI takes advantage of this directional dependence on diffusion and can map the orientation in space of white matter tracts assuming the direction of the fastest water diffusion indicates the overall orientation of the fibers (Basser PJ 1994) (Pierpaoli et al. 1996).

Diffusion Tensor Imaging Acquisition

In the original diffusion MRI method, diffusion is fully described using the diffusion coefficient, *D* (Le Bihan 1991). The effect of diffusion on the MRI signal is an attenuation *A*, which depends on *D* and on the "*b* factor" (Figure 3) which in turn depends on the gradient pulses used in the MRI sequence (Alexander et al. 2007).

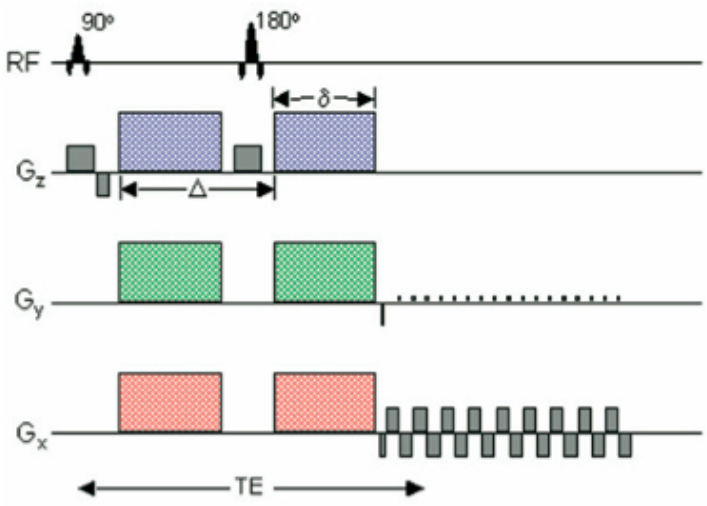

Figure 3. Schematic of a diffusion weighted echo-planar imaging pulse sequence (Alexander et al. 2007).

$$A = e^{(-bD)} \tag{2}$$

$$b = \gamma^2 G^2 \delta^2 (\Delta - \frac{\delta}{3}) \tag{3}$$

In the presence of anisotropy, diffusion cannot be characterized by a scalar coefficient, but requires a tensor matrix, **D**, to describe fully molecular mobility along each direction as well as the correlations between directions (Stejskal and Tanner 1965). The diffusion tensor is obtained from diffusion-weighted measurements in at least six non-collinear directions. The tensor is symmetric with six degrees of freedom, such that a minimum of six diffusion-encoded measurements is required to accurately describe the tensor. Using more than six directions will improve the accuracy of the tensor measurement for any orientation (Papadakis et al. 2000) (Hasan, Parker, and Alexander 2001). The tensor can be written in matrix form as

$$\mathbf{D} = \begin{bmatrix} D_{xx} & D_{xy} & D_{xz} \\ D_{yx} & D_{yy} & D_{yz} \\ D_{zx} & D_{zy} & D_{zz} \end{bmatrix} \tag{4}$$

Diagonalizing the matrix, the diffusion tensor can be written

$$\mathbf{D} = \mathbf{E}^{\mathbf{T}} \begin{bmatrix} \lambda_1 & 0 & 0 \\ 0 & \lambda_2 & 0 \\ 0 & 0 & \lambda_3 \end{bmatrix} \mathbf{E} \tag{5}$$

where **E** is a matrix of the eigenvectors describing the major, medium and minor principle axes of the ellipsoid (Figure 4) fitted to the data, and $\lambda_1, \lambda_2, \lambda_3$ are the eigenvalues for each eigenvector, which represent the diffusivity along each axis.

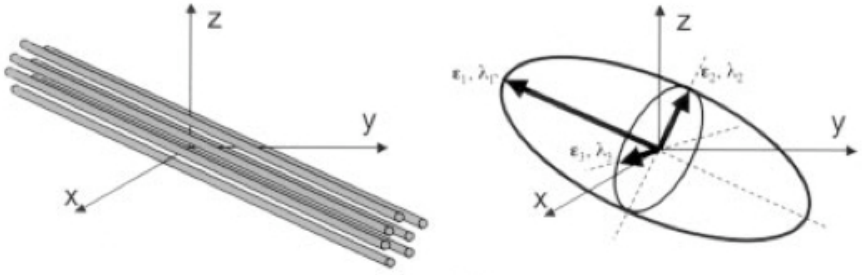

Figure 4. Tensor ellipsoid. Left, fiber tracts with an arbitrary orientation imposing anisotropic diffusion. Right, diffusion tensor ellipsoid characterized by the eigenvectors ($\varepsilon_1, \varepsilon_2, \varepsilon_3$), and eigenvalues ($\lambda_1, \lambda_2, \lambda_3$) (Jellison et al. 2004).

Diffusion anisotropy can be described as how much the shape of the tensor ellipsoid deviates from a sphere (Jellison et al. 2004). This is mathematically translated as to the degree which the three-tensor eigenvalues differ from one another.

Several invariant scalar indices made of combinations of the eigenvalues are used to characterize diffusion anisotropy, including apparent diffusion coefficient (ADC) and relative anisotropy (RA). The most widely used invariant measure of anisotropy is fractional anisotropy (FA) (Pierpaoli and Basser 1996).

$$FA = \sqrt{\left(\frac{3}{2}\right)\frac{(\lambda_1 - \bar{\lambda})^2 + (\lambda_2 - \bar{\lambda})^2 + (\lambda_3 - \bar{\lambda})^2}{(\lambda_1^2 + \lambda_2^2 + \lambda_3^2)}} \tag{6}$$

FA is a scalar value that ranges between 0 and 1. Increasing FA values indicate a higher tensor ellipsoid anisotropy.

FA, with no other information, is a highly sensitive but fairly nonspecific biomarker of neuropathology and microstructural architecture. This combination produces challenges to the interpretation of DTI measurements for both diagnostic and therapeutic applications. However, most agree that FA is a marker of white matter integrity.

Fibertracking

The orientation of the major eigenvector is assumed to be parallel to that of the local white matter tract, assuming the FA in the voxel of interest is above a certain threshold. These directional patterns can be displayed using color maps representing the three basic directions: red representing right-left, green representing anterior-posterior, and blue representing superior-inferior (Figure 5). Problems arise in regions of the white matter in which fibers cross or kiss. This reduces FA in the voxel and can misrepresent the fiber orientation.

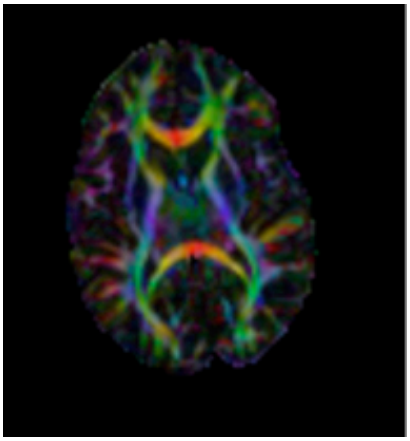

Figure 5. Colormap showing major eigenvector direction indicated by color (red: right-left; green: anterior-posterior; blue: superior-inferior)

Despite these complications, fibertracking is an important application in the visualization of anatomic connections between different parts of the brain on an individual basis. Connectivity studies are important for interpreting functional MRI data and establishing how activated foci are linked together through networks (Le Bihan et al. 2001).

Number Processing and Functional Magnetic Resonance Imaging

Several functional MRI studies have mapped the cognitive processes that occur during math visualization, comprehension, and computation. These studies have given great insight into how the human brain processes numbers and arithmetic operations.

Functional Imaging

Functional magnetic resonance imaging (fMRI) maps local physiological or metabolic consequences of altered brain electrical activity. FMRI methods can be made

sensitive to changes in regional blood perfusion, blood volume, and blood oxygenation. The most popular functional imaging method is blood oxygenation level dependent (BOLD) fMRI. The contrast in BOLD imaging is produced by the underlying metabolic activity of neurons, mainly from energy expended as a result of postsynaptic neuronal depolarization. The increase in metabolic need is met by an increase in blood flow to the localized area. It is unknown what exactly drives the increase in blood flow, however the most common belief is that it is a direct consequence of neurotransmitter action, thus reflecting local signaling (Matthews and Jezzard 2004).

BOLD imaging takes advantage of the fact that deoxyhemoglobin (deoxyHB) is slightly paramagnetic, which distorts the magnetic field in its vicinity. Vessels carrying oxygenated blood cause negligible distortion to the magnetic field, while capillaries and veins containing partially deoxygenated blood will distort the field to a greater extent. These microscopic field distortions cause interference from spins within this location. However, in a BOLD dependent imaging sequence, activated brain regions show an increase in signal. This is due to the local increase in blood supply, causing total oxygen extraction to decrease. This decrease in oxygen extraction increases the signal relative to baseline.

Numbers and Cognitive Functioning

An interesting question in neuroscience is how the brain can differentiate between two quantities, determine which quantity is larger, and manipulate these two quantities in different ways to obtain a new quantity. One theory suggests that evolution endowed the human brain with a predisposition to represent a number domain (Dehaene,

Dehaene-Lambertz, and Cohen 1998). This can be seen in children possessing a capacity for elementary number processing early in their development, prior to schooling or even the development of language skills (Spelke and Dehaene 1999).

Functional imaging has proven to be an invaluable asset in localizing the many areas of the cortex that aid in numerical processing and arithmetic computation. One of these regions is the horizontal segment of the intraparietal sulcus (HIPS), a major site of activation in studies of number processing (Chochon et al. 1999) (Pinel et al. 2001) . Chochon et al. showed HIPS activation when a subject was asked to subtract a one digit number from 11 and when asked to verbally name a number compared to verbally naming a letter. Pinel et al. showed HIPS activation during a task in which the subject was asked to determine if a single digit number was greater than a target number. Interestingly, activation occurred when the number was much greater or much smaller than the target (Figure 6).

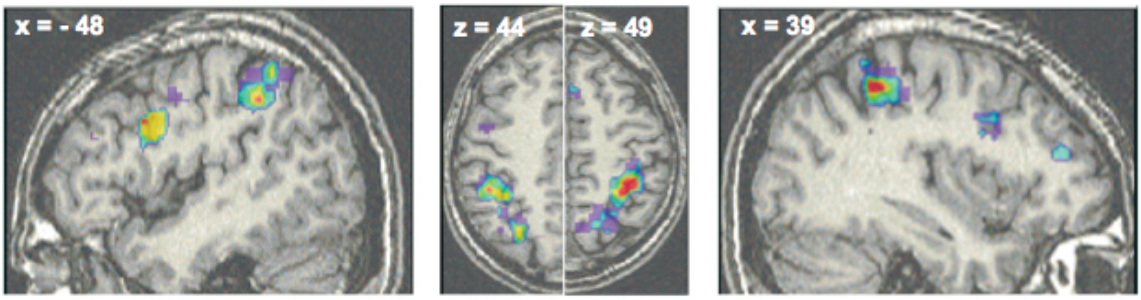

Figure 6. Activation of the horizontal segment of the intraparietal sulcus during number processing tasks This is average activation across several studies localizing activation in the intraparietal sulcus during number processing (Dehaene et al. 2003).

These studies suggest the HIPS is activated during mental calculations and number comparisons, and displays specificity for the number domain. The HIPS is more active when subjects calculate or compare two numerical magnitudes than when they

read numerical symbols (Cohen et al. 2000). The activation is also greater when a subject is asked to approximate a solution to an addition problem than calculating the exact solution (Dehaene et al. 1999). The HIPS has also been shown to have greater activation when processing numbers than processing other categories of objects on non-numerical scales, such as ranking animal sizes (Pesenti et al. 2000).

This activation of the HIPS is mostly bilateral, however the activation is greater in the right hemisphere during number comparison (Chochon et al. 1999). This suggests a right hemisphere advantage in comparison and other tasks requiring an abstraction of numerical relations (Dehaene et al. 2003). However, the parietal activation, although asymmetric, is usually present both hemispheres.

A second region, observed bilaterally in the posterior superior parietal lobule (PSPL), is also active in several tasks requiring number manipulations (Figure 7). This region is posterior to the HIPS. This regions has been shown to be active during number comparison (Pesenti et al. 2000), approximation (Dehaene et al. 1999), subtraction of two digits (Lee 2000), and counting (Piazza et al. 2002). This region increases activation when subjects carry out two operations instead of one. Although this region displays activation during many numerical tasks, it is not specific to the number domain. It also plays a role in a variety of visuospatial tasks such as hand reaching, eye orientation, and spatial working memory (Corbetta et al. 2000).

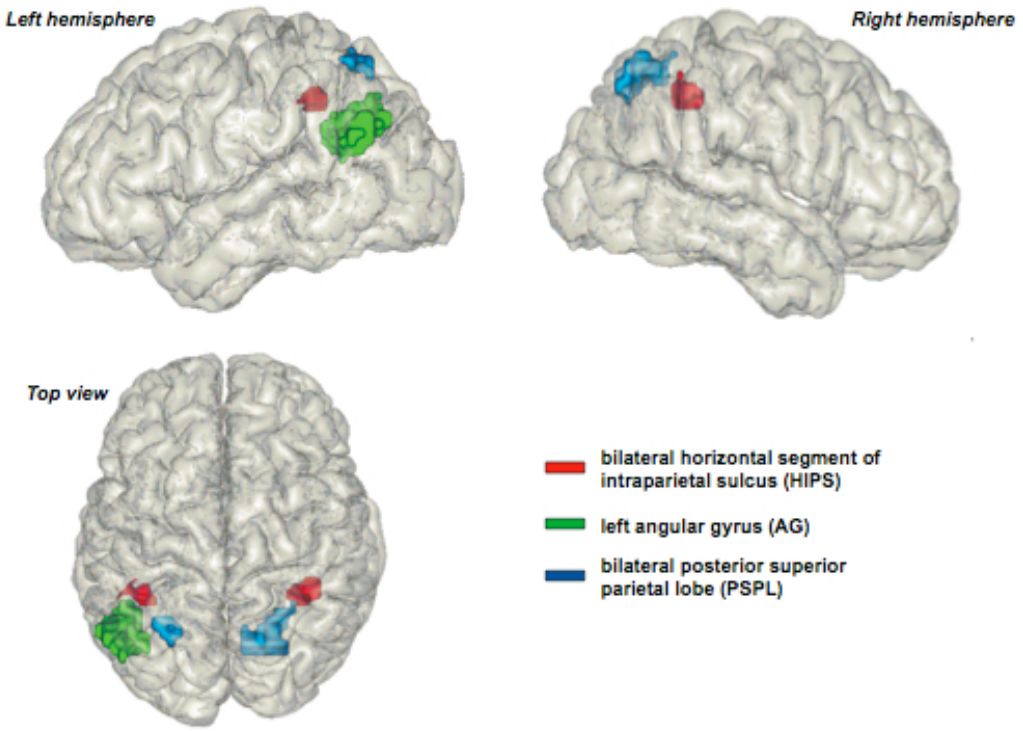

Figure 7. Representation of parietal region activation during number processing. The left angular gyrus is mostly activated during verbal representation of numbers (Dehaene et al. 2003).

A study by O'Boyle et al. showed that mathematically gifted male adolescents showed a higher activation in these parietal brain regions during 3-dimensional mental rotations than a control group of male adolescents (O'Boyle et al. 2005) (Figure 8). Three-dimensional mental rotation is a complex visuospatial task that highlights the engagement of at least two fundamental cognitive processes: the creation and manipulation of mental images (Hill, O'Boyle, and Hathaway 1998). These capacities have been shown to be useful when applied to mastery of high-level mathematical thinking and reasoning.

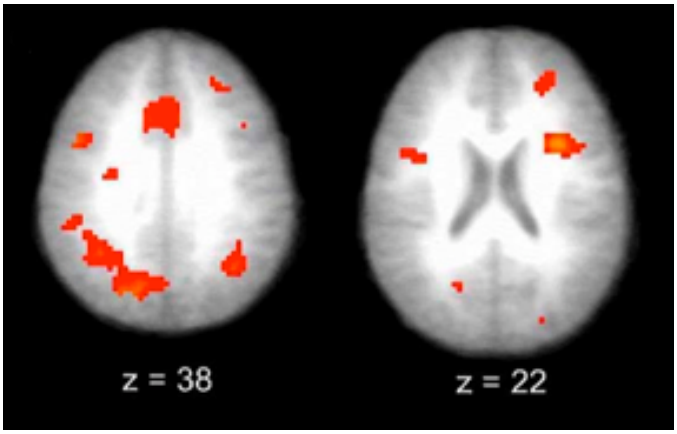

Figure 8. Significant activation during mental rotation in two axial slices. These images illustrate the regions having significantly greater activation in the math-gifted group. The largest activation occurs in the left parietal cortex (O'Boyle et al. 2005).

Diffusion Tensor Imaging and Reading

Although there are no current publications on mathematical processing and DTI, there are several papers relating reading ability and the microstructure of white matter using DTI. These studies are important in that it is possible that numerical processing and reading may have similar cortical locations, but may utilize similar or different white matter tracts. These neural pathways for reading and reading comprehension are better understood than the neural networks of number comprehension and mathematical computation, and thus give a foundation of how to study neural networks for number processing.

Klingberg et al. published the earliest paper relating reading ability and white matter microstructure (Klingberg et al. 2000). This study was done as a result of findings that suggested that developmental dyslexia may represent a disconnection syndrome in which communication is impaired between cortical areas involved in reading. Horwitz et al. found that dyslexic individuals exhibit decreased correlations of cortical activity

between the angular gyrus and inferior frontal, extrastriate occipital, and temporal areas (Horwitz, Rumsey, and Donohue 1998). Klingberg et al. hypothesized this disruption was possibly located in white matter tracts connecting temporo-parietal and frontal cortices. The study found that poor reading was associated with lower anisotropy in two regions of the brain, located bilaterally in the white matter of the temporo-parietal region (Figure 9). The lower anisotropy in this region is presumably due to differences in the number of axons, thickness of axons, amount and integrity of myelin, or structural disruptions of the white matter tracts.

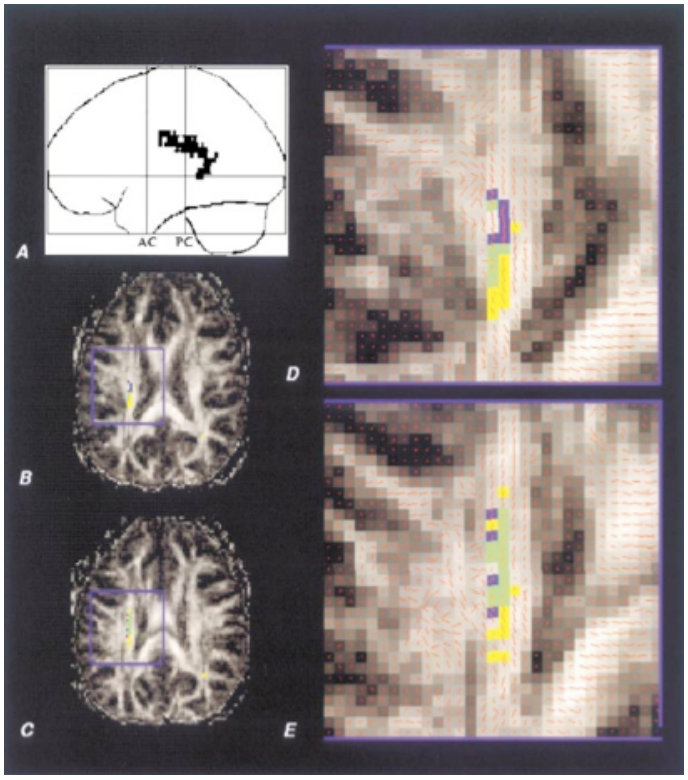

Figure 9. Regions with group differences in anisotropy and correlations with reading scores. (A) Sagittal projection of left hemisphere showing voxels with significant difference in anisotropy. (B) and (C) Two different axial slices showing voxels with significant differences. (D) and (E) Regions of interest from (B) and (C) magnified (Klingberg et al. 2000).

Once the group differences in anisotropy were found, a correlation analysis was done to find voxels in the white matter with significant correlation between anisotropy and performance on a reading test. This analysis found only one cluster of voxels in the left hemisphere that overlapped with their cluster from the group anisotropy study (Figure 10). These results suggested that white matter underlying left temporo-parietal cortex plays a critical role in reading ability.

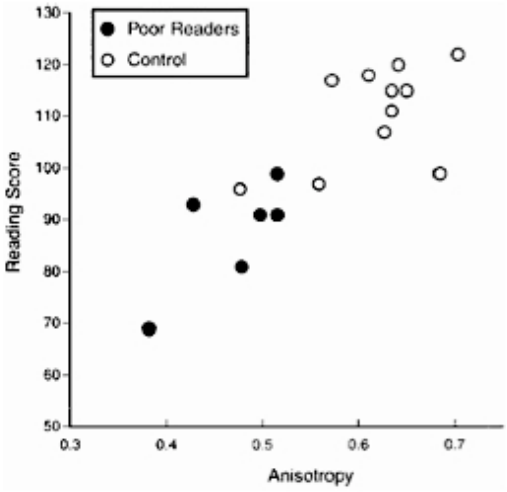

Figure 10. Plot of anisotropy versus reading score in the voxel with the highest correlation with reading score (Klingberg et al. 2000).

Beaulieu et al. was the first group to study the relationship between reading ability and white matter microstructure using DTI in children (Beaulieu et al. 2005). They believed that studying adults was informative, but the findings could be due to a lifetime of reduced reading or adaptive compensation mechanisms. They wanted to determine whether the neural differences were present at an earlier age during neurodevelopment, which includes a critical period for intervention. The 32 volunteers for the study had a

mean age of 11.1 years. The group performed a voxel-by-voxel correlation analysis of FA with reading ability based on the Word Identification subtest of the Woodcock Reading Mastery Test. They found five clusters of voxels that positively correlated with reading ability, the largest of which was located in the left temporo-parietal white matter (Figure 11) (Figure 12).

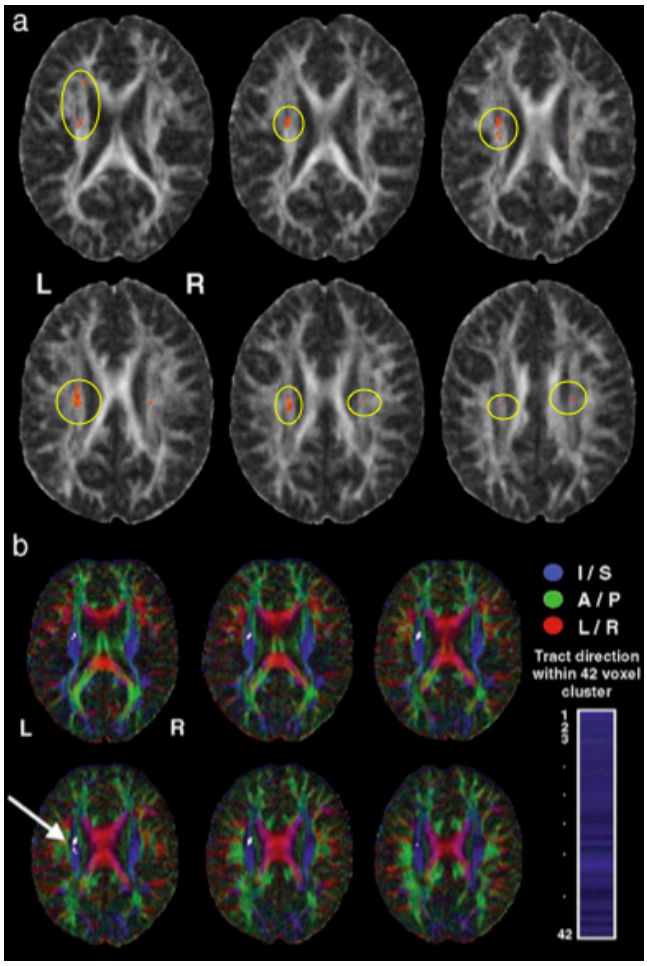

Figure 11. White matter correlation of FA and reading ability. (a) All voxels of the five significant clusters in red (circled). (b) Diffusion tensor derived color maps, arrow points to largest cluster comprised in tracts in the inferior-superior orientation (Beaulieu et al. 2004).

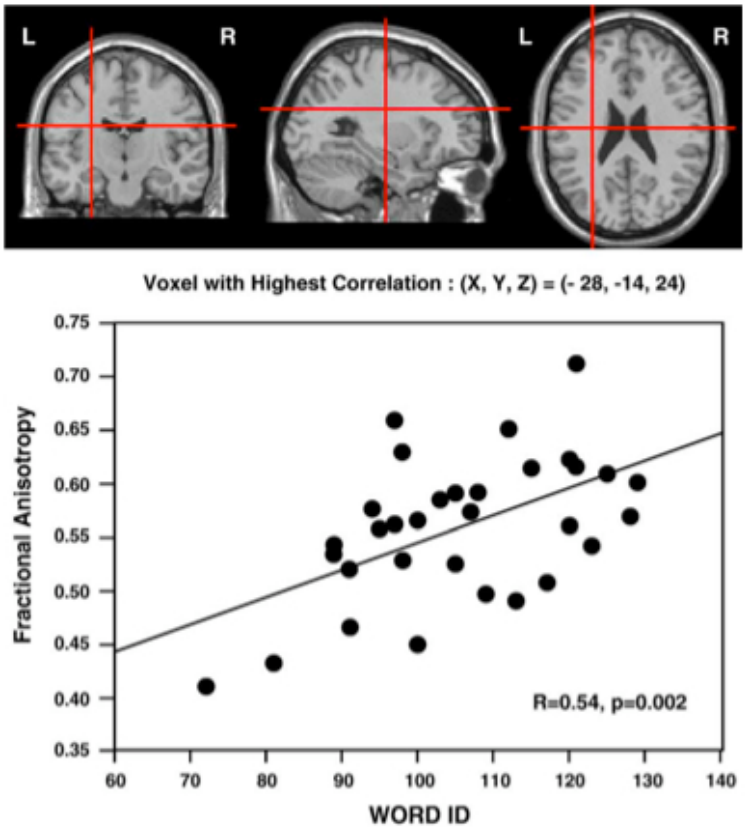

Figure 12. FA versus reading ability in the most correlated voxel. Top image depicts anatomical location of voxel (Beaulieu et al. 2004).

Beaulieu et al. also provided tractography of white matter fibers that passed through each of the five significant clusters. Three smaller clusters in the left hemisphere have anterior-posterior tracts consistent with the superior fronto-occipital fasciculus and anterior limb of the internal capsule or left-right tracts consistent with the corpus callosum. The largest cluster and the cluster in the right hemisphere have superior-inferior tracts consistent with the posterior limb of the internal capsule. The authors hypothesized that these two clusters are part of the superior longitudinal fasciculus (SLF), which is thought to be a critical white matter track connecting the language regions of Wernicke and Broca. They found that the largest cluster was bordered on the lateral side

by the SLF. They believe this cluster could have crossing white matter tracts inside of it, but their experiment could not resolve these fiber crossings (Figure 13).

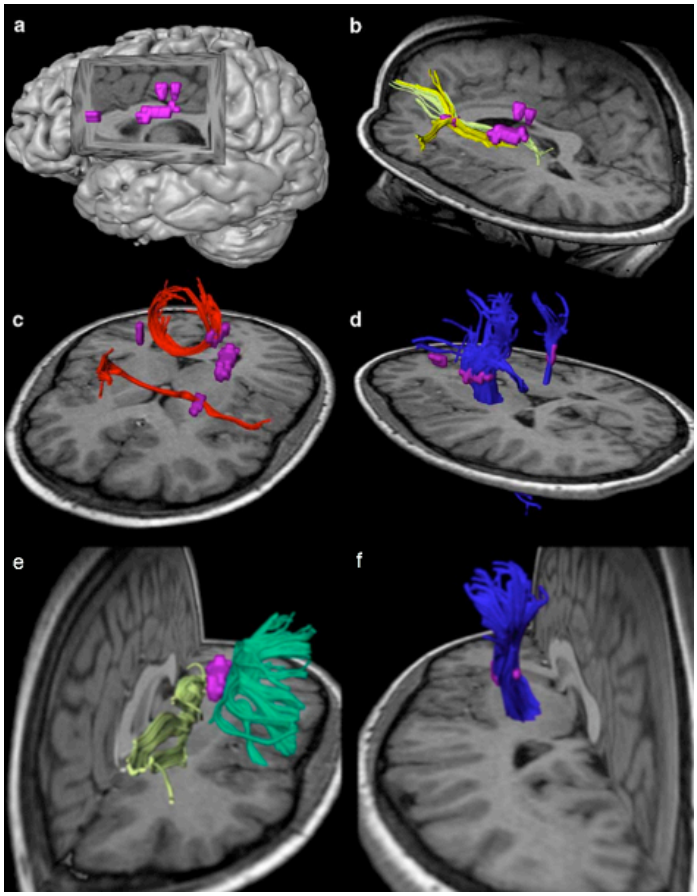

Figure 13. Fibertracts passing through clusters. (a) The five clusters used as seed points. (b) Anterior-posterior fiber, (c) left-right fibers, and (d) superior-inferior fibers. (e) Fibers directly medial (yellow) and lateral (green) to the largest cluster. The green fiber is the SLF. (f) Fibers passing through the largest cluster, which is part of the posterior limb of the internal capsule (Beaulieu et al. 2004).

Several investigators have used fiber tracking to determine the major white matter tracts that display correlations with reading ability. These regions are the posterior limb of the internal capsule (Beaulieu et al. 2004), part of the corona radiata, the left SLF (Klingberg et al. 2000) (Niogi and McCandliss 2006), and the corpus callosum (Beaulieu et al. 2004) (Figure 14).

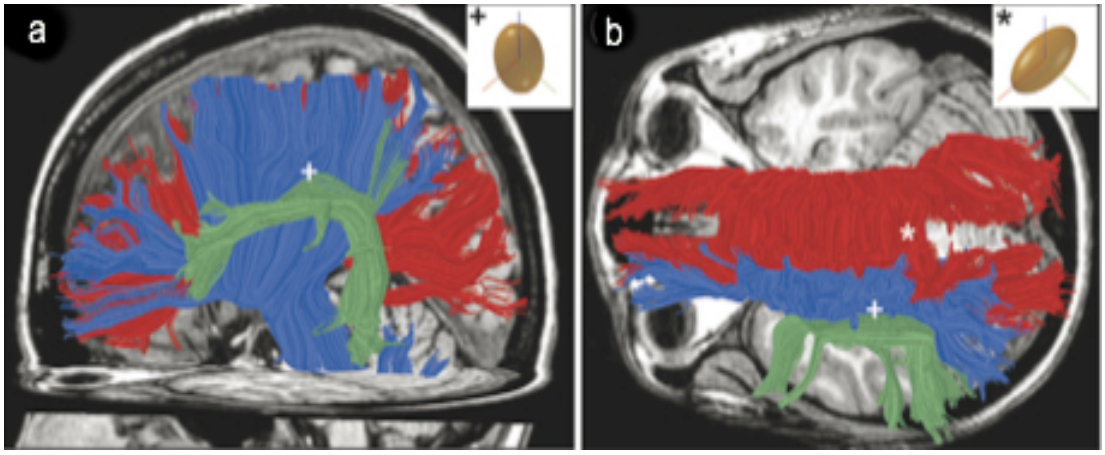

Figure 14. Major fibertracts in DTI studies of reading. (a,b) Fibertracking estimates of the SLF (green), corona radiata (blue), and corpus callosum (red) from a sagittal view of left hemisphere and axial view from above. Insets show diffusion tensor ellipsoid at the of the corona radiata (+) and in the posterior callosum (*) (Ben-Shacher et al. 2007).

It is poorly understood why fibers in the corona radiata would be correlated with reading ability, however one study suggests that the corpus callosum plays a key role. One option is that there are differences in the corpus callosum in those with reading difficulties, including enlargement of the splenium (Rumsey et al. 1996) (Robichon and Habib 1998). This enlargement causes fibers in the corona radiata to be displaced, altering the diffusivity in those voxels occupied by the corona radiata. The second theory is that differences in callosal fibers that interdigitate with the corona radiata might change the diffusivity measurements inside the corona radiata. Differences between poor and good readers in either size or number of these callosal fibers can produce FA differences in voxels where callosal fibers pass though the corona radiata (Ben-Shachar, Dougherty, and Wandell 2007).

Current Study

In this study, we evaluate regions of the white matter that may show microstructural differences between children with normal math abilities and those with math difficulties. By evaluating these regions, we can begin to understand the neural pathways being used during math computation. A better understanding of the white matter structures showing lower FA will help determine a course of intervention for children with similar math difficulties. Fibertracking of these regions will aid in proper identification of white matter fibers and will determine connectivity profiles of cortical regions activated during certain math tasks.

This study also investigates white matter regions that show microstructural differences related to reading ability. This is done to determine the microstructural relationship between reading and math computation abilities.

CHAPTER II

METHODS

Child Recruitment and Screening

Subjects were recruited to this study from a pool of children participating in a larger study investigating the effects of mathematics problem-solving instruction. This larger study recruited children from seven schools in a southeastern metropolitan school district. Parents of children participating in the larger study received a letter from the child's teacher with information about the imaging study. Parents interesting in having their child participate in the study gave consent to be contacted by the imaging researchers. Thirty-three children were included in the imaging study.

Trained examiners administered the calculation and reading subtests of the Wide Range Achievement Test – Third Edition (WRAT-3) in the fall of the child's third grade year (Gary Wilkenson 1993). The WRAT-3 is a widely used standardized measure of achievement. The calculation subtest involves many aspects of math computation, including number comparisons, counting, and number identification. The reading subtest assesses the recognition and naming of letters and words out of context.

Performance on these tests was used to classify the children into three groups: control, math difficulty (MD), and reading and math difficulty (MD/RD). Children who performed below the 20th percentile on the math test were placed in the MD group, while children who performed below the 20th percentile in both tests were placed in the MD/RD group(Table 1)(Table 2).

Table 1. The number of children in the control, math difficulty (MD), and math and reading difficulty (MD/RD) groups.

Group	N
Control	21
MD	3
MD/RD	9

Table 2. Mean scores on the WRAT-M and WRAT-R in control, math difficulty, and reading difficulty groups.

Group	WRAT-M	Group	WRAT-R
Control	108.6 +/- 6.1	Control	114.2 +/- 11.6
MD	81.7 +/- 12.9	RD	77.7 +/- 12.8

Imaging

Diffusion Tensor Imaging

To prepare for the MR scan, the participants were placed in a mock scanner to acquaint them with the scanning process. They also practiced the types of math problems they would encounter during the fMRI scans. Once the participants were comfortable with the setup, the actual scanning commenced in a 3 Tesla Philips Achieva MRI scanner. An anatomical T1-weighted, 3D-TFE-SENSE sequence was done with a resolution of 256 x 256 x 170 mm and a voxel size of 1 x 1 x 1 mm. An additional participant not involved with the current study also was scanned with this anatomical sequence; this dataset would be the target used for the registration process. Diffusion Tensor images were obtained for each participant using an EPI-SENSE sequence with a matrix size of 128 x 128 x 60 mm and a voxel size of 2 x 2 x 2 mm. The DTI sequence acquired images with diffusion-weighting applied in 32 non-collinear directions with a b-

value of 1000 s/mm^2 and another image with zero diffusion weighting. Most of the participants had two full DTI scans, however a few had one DTI scan.

Functional Imaging

The participants were asked to do several math tasks in the magnet (Figure 15). They were given a problem and asked to push a button that corresponded to the correct answer. The fMRI run was five minutes in length and consisted of three 40-second blocks of each numerical task, three 40- second blocks of the control task, and three 20-second blocks of rest. During the blocks of numerical tasks, the math problem would appear on the screen and the possible answers would appear 1000 msec later. The problem and possible answers remained on the screen until the participant responded or the imaging block ended after 40 seconds. The control task consisted of two non-numerical Greek symbols represented in the same manner as the numerical tasks and three other non-numerical Greek symbols appearing 1000 msec later. The participant had to identify the matching symbol. The participant's answer and reaction time were recorded.

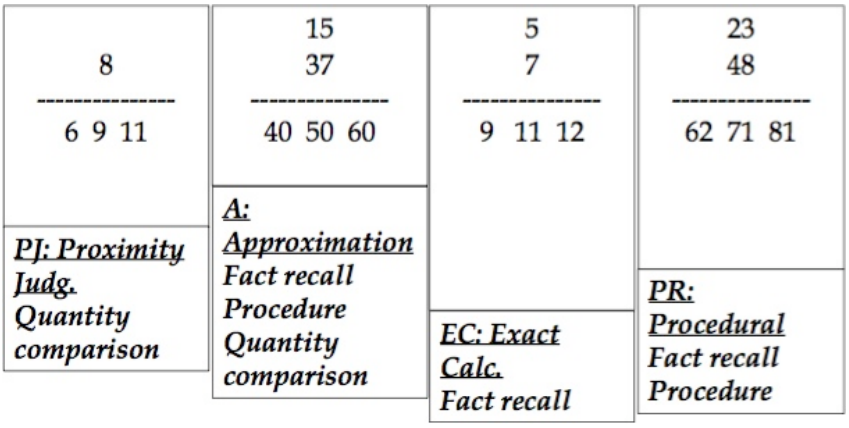

Figure 15. The four types of math tasks presented during fMRI scans. Proximity judgment asks the participant to choose the number closest to that presented. Approximation asks the child to add two numbers and choose the answer that is closest to the correct sum. Exact calculation asks the participant to add two single-digit numbers and choose the answer that is the sum of the numbers. Procedural calculation asks the participant to add two double-digit numbers and choose the answer that is the sum.

Image Processing

Once the images were obtained, the datasets were uploaded from the scanner to the server. The diffusion and anatomical datasets were pre-processed prior to making quantitative measurement. Pre-processing included procedures that corrected for eddy current and motion artifacts, skull-stripping of the 3-D anatomical datasets, rigid and non-rigid intra-subject registration, rigid and non-rigid inter-subject registration, and dataset mapping. All of these steps are necessary to guarantee sufficient image quality for statistical analyses on the datasets.

Eddy Current and Motion Correction

Two of the largest problems associated with DTI are the artifacts created by eddy currents and bulk motion. Eddy current induced geometric distortion depends on the magnitude and direction of the field gradients (Jezzard, Barnett, and Pierpaoli 1998). Eddy currents are produced when strong gradient pulses are switched rapidly (Le Bihan et al. 2006). When diffusion gradient pulses are switched on and off, the time varying magnetic field results in current induction in the conducting surfaces of the MR scanner. This sets up magnetic field gradients that may persist after the primary diffusion gradients are off. These added gradients are proportional to the strength of the primary diffusion gradients. The result is that the actual gradients experienced by spins in the tissue are not exactly the same as those programmed to produce and reconstruct the image. This creates three types of image distortions: image shearing, image scaling, and bulk shifting (Figure 16). These distortions of the individual diffusion weighted images produce misregistration artifacts in maps of diffusion parameters. This results in lower spatial resolution of computed maps and an inaccurate estimation of diffusion parameters (FA, ADC) at boundaries between tissues.

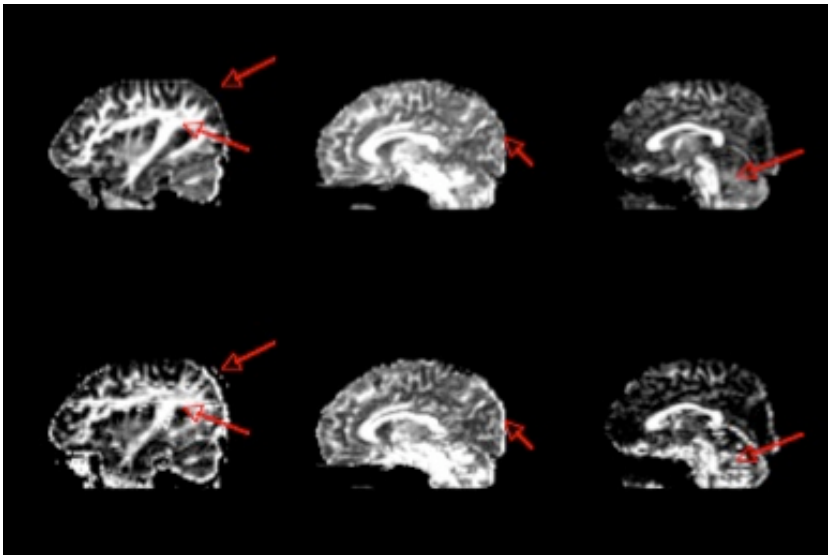

Figure 16. Eddy current correction. Each column represents a single dataset. The bottom row represents the uncorrected images while the top row depicts the corrected images. Arrows point to the regions most affected by eddy currents.

In order to create diffusion-weighted contrast, pulse sequences must be sensitive to molecular motion on the order of a few micrometers. Because of this sensitivity, bulk motion is a large problem. Small movements during the phase-encoding portion of the scan will cause large phase changes in the echo signal (Bammer 2003). Because each echo will most likely capture different phase errors, patient motion produces ghosting errors.

Each dataset was corrected for motion and eddy current artifacts using PRIDE (Philips Research Integrated Development Environment) software written in Interactive Data Language (ITT Visual Information Solutions, Boulder CO). This program corrects eddy current and motion artifacts in each image and performs registration of each image to a common space. In the case that an exam had two DTI scans, the diffusion

registration program corrected for distortions, registered, and averaged the two scans together.

Extraction of FA Maps

The distortion corrected datasets were then read by the Philips PRIDE fibertracking program. This program calculated the tensor and associated diffusion parameters in each image voxel. FA maps were generated for later statistical analyses.

Skull Stripping of Anatomical Datasets

The 3-D anatomical datasets were skull-stripped using the Brain Extraction Tool (Smith 2002) from the freeware software MRIcro (Rorden and Brett 2000). This tool enables the user to specify how much of the scalp, underlying fat, and skull they wish to remove simply by changing a factor between 0 (removes much tissue) and 1 (does not remove any tissue). After trying several brain removal factors, most of the datasets were processed using a .4 factor, however some datasets required a .5 factor.

Skull stripping is necessary for image registration, specifically non-rigid registration. The registration algorithm attempts to align the top of the non-diffusion weighted image (b=0), used to map the DTI dataset to the target space, with the top of the skull in the T_1-weighted image, which will result in misalignment of the datasets. Skull stripping ensures that the top of the brain from the b=0 dataset will align with the top of the brain in the anatomical dataset (Figure 17).

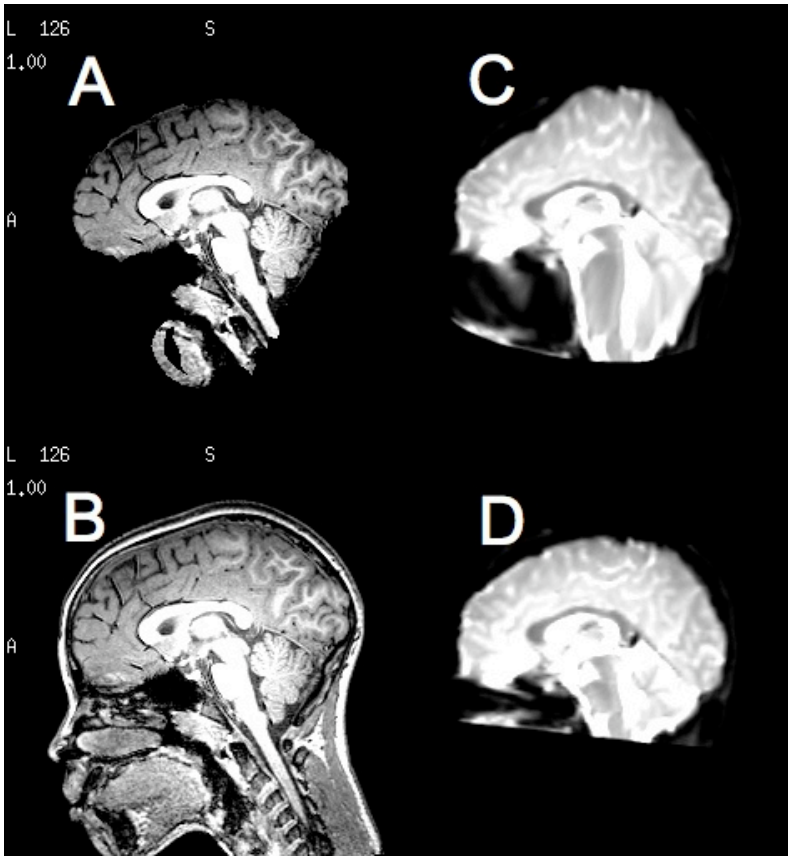

Figure 17. Skull-stripping. (a) Skull-stripped image, (b) original T1-3D image, (c) attempt at registering a b-0 image to non-skull-stripped T1-3D image, (d) attempt at registering a b-0 image to skull-stripped T1-3D image.

Image Registration

In order to make comparisons between subjects, the images must be mapped onto a common space. That is, each voxel from each dataset must represent the same anatomical location on each participant. For example a voxel in the corpus callosum in one dataset must have the same location in the corpus callosum across all datasets. This is done by applying rigid and non-rigid registrations to transform each dataset to a commons space, represented by the anatomical dataset from the participant not in the remainder of the study.

Rigid registration involves translation and rotation. One image is translated and rotated to find the best fit to a target image. There are many algorithms that try to minimize the registration error between the two images. This study incorporated an algorithm that maximizes mutual information (Li 2001). Mutual information (MI) measures the statistical dependence between two random variables or the amount information that one variable contains about the other. The MI of the image intensity values of corresponding voxel pairs is maximal if the images are geometrically aligned (Maes et al. 1997). There are many input paramters that control the program, including the minimum and maximum intensity of the target and reference images, number of bins to be used in the histogram, optimization order, and sampling intervals (Figure 18).

Figure 18. Example of rigid registration. (a) Original 3D image to be registered. (b) Target image. (c) Original image registered onto target image.

Non-rigid registration warps the image in a non-linear fashion and thus does not maintain the spatial coherence of the image. This registration is much more complex and time consuming, however it is an essential step to ensure a homogenous map across all subjects. This study uses the Adaptive Bases Algorithm developed at Vanderbilt University (Rohde, Aldroubi, and Dawant 2003) (Figure 19).

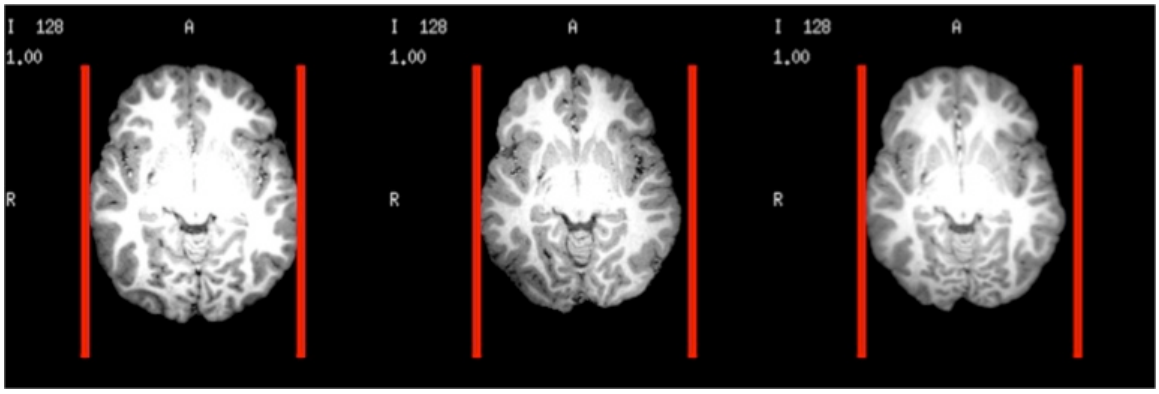

Figure 19. Example of non-rigid registration. (a) Original 3D image. (b) Target 3D image. (c) Original 3D image after Adaptive Bases Registration. The red lines depict the width of the original image to show how non-rigid registration warps.

The first step in the registration process is to obtain the non-diffusion weighted (b=0) image from the DTI data from each dataset. This image is rigidly registered to the subject's own anatomical 3D image. This b=0 image has a resolution of 128 x 128 x 60 mm and a voxel size of 2 x 2 x 2 mm, while the 3D anatomical images have a resolution of 256 x 256 x 170 mm and a voxel size of 1 x 1 x 1mm. This registration program interpolates the b=0 image data so that it has the same resolution and voxel size as the 3D anatomical datasets. The translation optimal vector and rotation matrix for rigid registration are saved for future use. The output of this rigid transformation is then registered to the same 3D image using the non-rigid Adaptive Bases Algorithm. The deformation fields obtained from the non-rigid registrations are saved for future mapping. After registration, each image is visually inspected to ensure accuracy. If the registration errors are too large, the configurations for each registration algorithm are adjusted, usually by adjusting intensity values or the jacobian threshold, and the registrations are rerun.

The b=0 maps for each subject are now in the subject's 3D anatomical space. In order to get every subject's dataset in the same space, the 3D anatomical images must be

registered to a common 3D anatomical space. A 3D anatomical image was obtained from a child that was not a participant in the DTI study. This dataset defines the common 3D anatomical space. Each subject's 3D anatomical dataset is rigidly and non-rigidly registered to this common 3D space. The deformation field, translation vector, and rotation matrix are saved for future transformation of the FA maps (Figure 20).

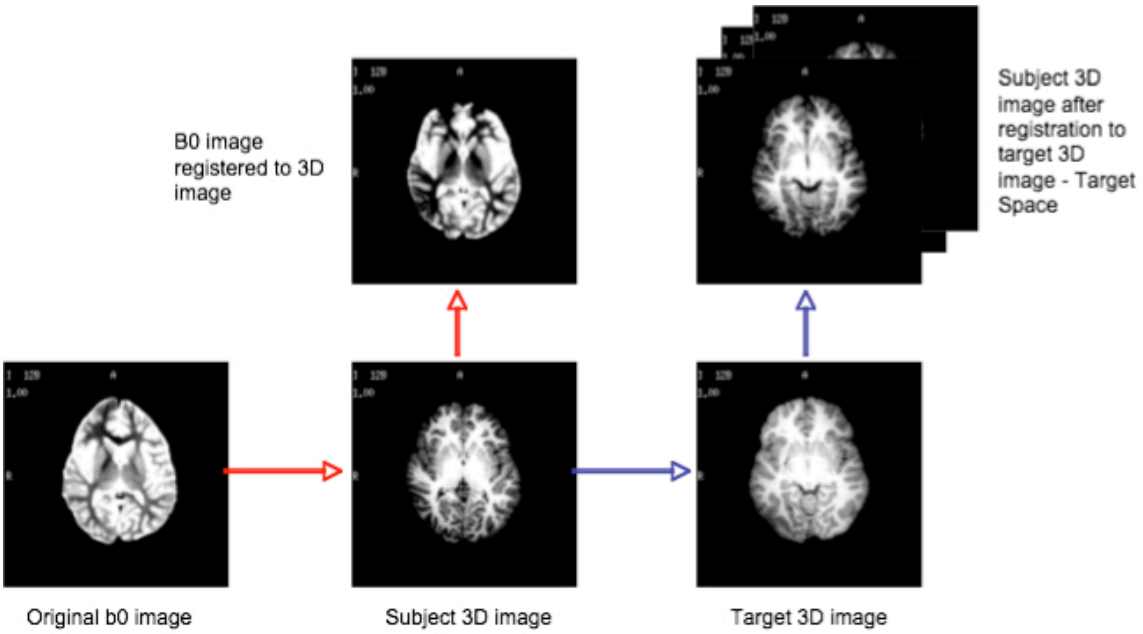

Figure 20. The registration process from the b=0 image to the common target space. Each arrow indicates a rigid and non-rigid registration.

The saved deformation fields, translation vectors, and rotation matrices are important in that they define how the FA data are transformed onto the target space. Once each subject's FA data are mapped onto the target space, the FA datasets from each subject are decimated back to a resolution of 128 x 128 x 85 mm and are averaged using MATLAB© to create an average FA map across all subjects. This averaged FA map is then used as a target for another registration step. This registration takes each subject's original FA data and maps them onto this common, averaged FA space. This step has

been shown to improve overall registration errors. The deformation fields are applied to the subject's original FA data. The FA data are now in a common space and ready to be analyzed.

Statistical Analysis

Once each FA map is registered to a common space, the participants were separated according to their WRAT-Math (WRAT-M) scores. Those that scored above 100 were placed in the control group, while those that scored below 80 were placed in the math difficulty group (MD). These groups were made so that a t-test comparison could be done between the two groups. Those that had a WRAT-M score between 80 and 100 were placed in a buffer group and were not included in the t-test. A two-sample t-test was done on a voxel by voxel basis using MATLAB©. The t-statistic and p-value were saved for each voxel in the image volume. Regions-of-interest (ROIs) were found by applying a threshold on the statistical maps. Those voxels that had $p<.05$ and a positive t-statistic were deemed voxels in which the control group had FA values that are statistically higher than the MD group. Voxels that fit these criteria were placed into an ROI only if they were part of a cluster of at least six continuous voxels. Any cluster smaller than 5 voxels was not included in further analysis. These ROIs were then mapped onto the average FA map to determine the location of the ROI. Any region that was in the middle of a large white matter tract was further analyzed, while those that were in gray matter, or on the edge of a white matter tract were discarded due to possible registration errors. Once these regions were identified, the x-y-z coordinates of the ROI were found in order define as seed points for fibertracking.

To determine the relationship between FA and the WRAT-M scores, a linear correlation was performed with the entire cohort (MD, buffer, and control groups). The correlation was done on a voxel by voxel basis using MATLAB©, which created maps of the p-value and correlation coefficient for each voxel. To determine regions of interest, a threshold of $p<.05$ and $r>.3$ was placed on each voxel. Voxels that fit these criteria were placed in an ROI only if it was part of a cluster that was at least six pixels in size. This process was repeated to determine the relationship between FA and WRAT-R scores. The ROI's for WRAT-M and WRAT-R were displayed with different colors on an average FA map to determine location and overlap. Any ROI in gray matter or on the edge of a white matter tract was not included in further analysis. Once these regions were identified, their x-y-z coordinates were found in order to define seed points for fibertracking.

Correlation analysis was also performed relating each subject's FA map to fMRI activation during the four in-magnet tasks performed by each participant. The fMRI activation is quantified by the relative signal change in a particular region associated with task performance. The higher the coefficient, the more activation there was in the region. Activation in several regions were taken from the parallel fMRI study to determine the relationship between FA and cortical function. A voxel-by-voxel correlation was performed in MATLAB© between each subject's activation and FA value. A statistical p-value map was created and ROI's were found using a threshold of $p<.05$ and a cluster size of 6. Any ROI deemed to be in gray matter or on the edge of a white matter tract was not included in further analysis. Once the regions were found, the spatial coordinates were found in order to define seed points for fibertracking.

Once all of the regions had been found for all tests, they are mapped onto each subject's individual FA map in the common space. This masks out each region in order to find the FA values for that particular region and subject. The mean FA of the ROI for each subject is recorded. These FA values are used to determine the relationship between FA scores and the participant's performance on the in-magnet tasks using SPSS®.

Fibertracking

It is often difficult to determine the anatomical location of an ROI judging from a two-dimensional image FA. It is useful to use this ROI as a seed point for fibertracking. The ROI coordinates are found, and a backwards deformation field is applied. This converts the ROI coordinates back into the subject's native DTI space, where fibertracking can take place. A control's DTI dataset was used to do the fibertracking of all the seed points. Once these regions are mapped onto the native DTI space, the PRIDE fibertracking tool takes the information from the DTI scans (direction vectors and FA values) and 'steps' in the direction of the fiber. The program keeps tracking the fiber until either the fiber changes direction at an angle that is too steep, or the FA value falls below a certain threshold. The FA threshold that was used for this study was .25.

Each region was used as a seed point and a tract was found for each case. If there was reason to believe that two regions were connected by a fiber, then the two regions were entered as seed points and the program only found fibers that crossed through both seed points. Fibertracking aided greatly in identifying the anatomy of the ROI's found in the statistical analyses.

CHAPTER III

RESULTS

Many white matter regions were found to correlate with WRAT-M scores, WRAT-R scores and functional imaging coefficients. Each ROI is mapped onto a averaged FA map in the sagittal plane. The slices are numbered from 1 to 85, with the first slice being the left side of the brain and 85 the right.

Sagittal Slices

Slice 24

The first region was found in the left parietal lobe of the brain, based on the linear correlation analysis (Figure 21). The t-test between the control and math difficult groups confirms a region in the left parietal area that shows the FA values are significantly higher for the control group than the math difficult group (Figure 22). An anatomical dataset confirms the location of the ROI (Figure 23). Using this region as a seedpoint for fibertracking produces a fiber that runs in a horseshoe pattern into the cortex of the left parietal area of the brain (Figure 24). A second branch protrudes from the seedpoints and is believed to be part of the inferior longitudinal fasciculus.

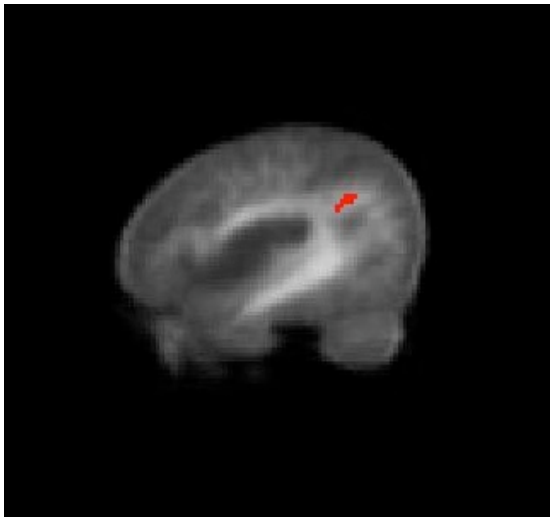

Figure 21. Region (red) in which FA correlates FA with WRAT-M scores.

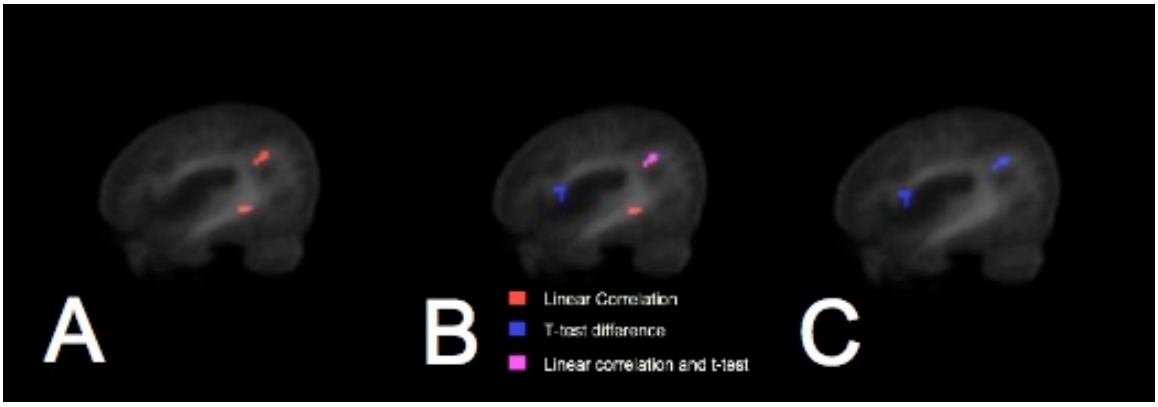

Figure 22. Group t-test and linear correlation analyses. (a) Regions found using linear correlation technique correlating math score with FA, (b) regions found from both t-test and linear correlation with red regions indicating linear correlation test, blue regions found using the t-test, and pink regions indicating regions were there is a linear correlation between FA and math scores and the control group has a significantly higher FA score than the math difficult group according to the t-test, (c) regions where the control group has significantly higher FA scores than the math difficult group.

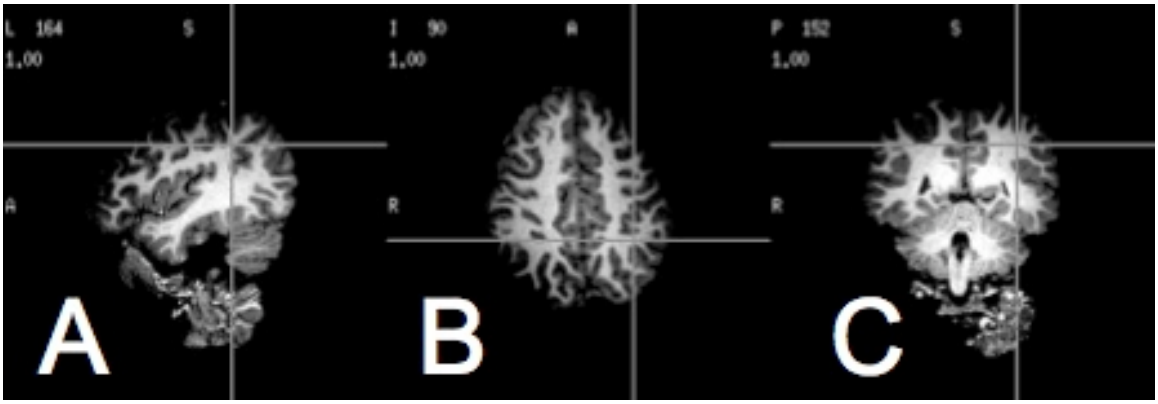

Figure 23. Anatomical location in (a) sagittal, (b) axial, and (c) coronal planes of ROI in left parietal lobe where FA is correlated with WRAT-M.

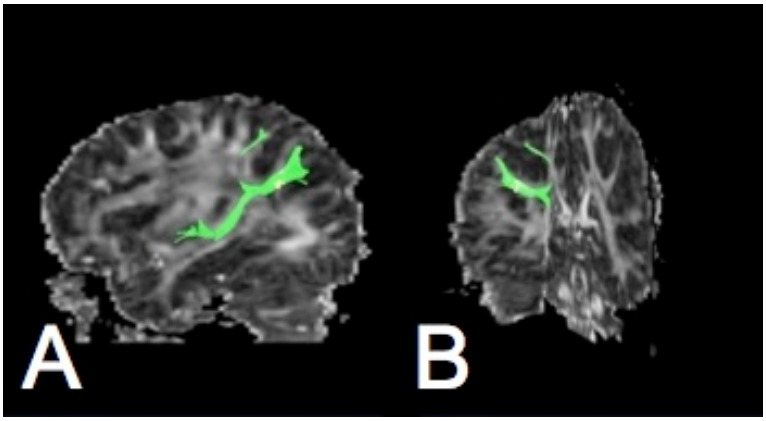

Figure 24. Fibertract (green) using left parietal region (see Figure 21) as seedpoint (yellow). (a) Sagittal view, (b) 3D view. One fiber runs in a horseshoe orientation to the corttex of the left parietal lobe. A second fiber is part of the ILF.

This same slice also included regions that showed a relationship between FA values and the WRAT-R scores (Figure 25). One of the regions is found to be correlated with both WRAT-M and WRAT-R scores, which fibertracking confirms is part of the ILF. A reading only region is also found in the superior longitudinal fasciculus, which is confirmed by fibertracking.

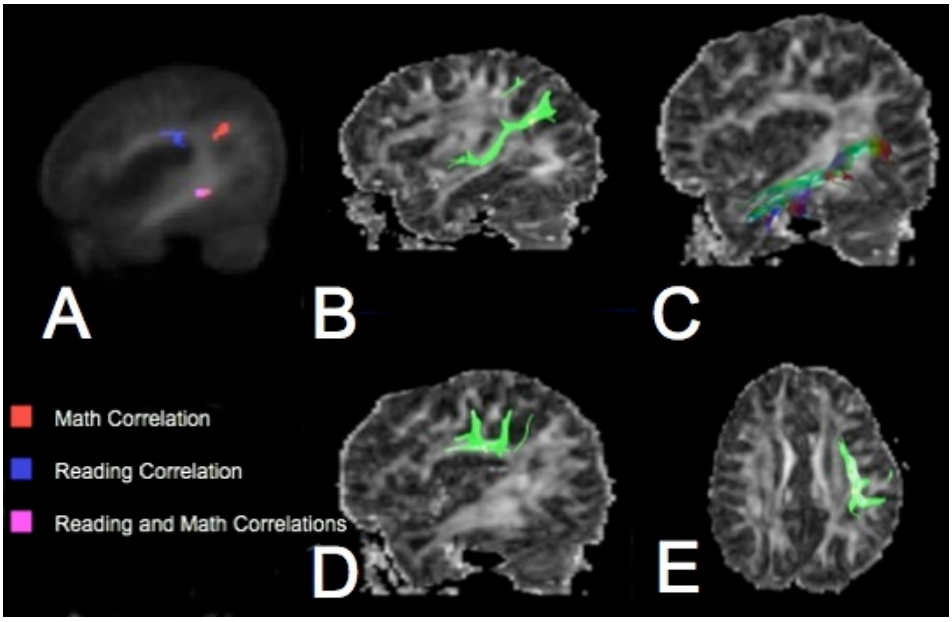

Figure 25. Regions in which FA correlated with math and reading, with corresponding fibertracts. (a) Regions correlated with reading (blue), math (red), and both reading and math (pink). (b) Tract of math region in left posterior lobe, (c) tract of region correlating with both reading and math indicating inferior longitudinal fasciculus, the color of the tract indicates fiber direction, (d) sagittal view of tract through the reading region that is part of superior longitudinal fasciculus, (e) axial view of reading tract.

Slices 26-28

The second region found that correlates FA with WRAT-M scores is shown in the left occipital region of the brain (Figure 26). This region is relatively large as it is found in three consecutive slices (Figure 27). Fibertracking confirms the location of this ROI (Figure 28).

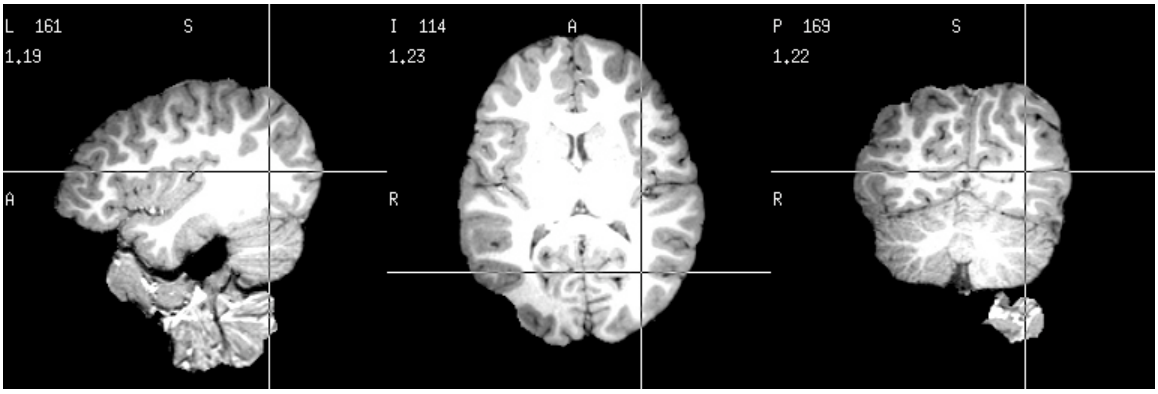

Figure 26. Anatomical location of region found in left occipital lobe correlating FA with WRAT-M.

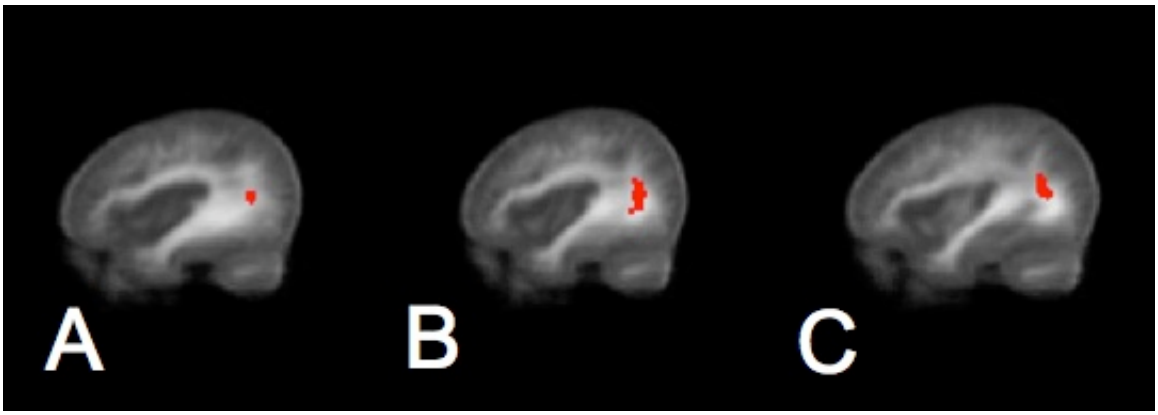

Figure 27. Region correlated with WRAT-M in (a) slice 26, (b) slice 27, and (c) slice 28).

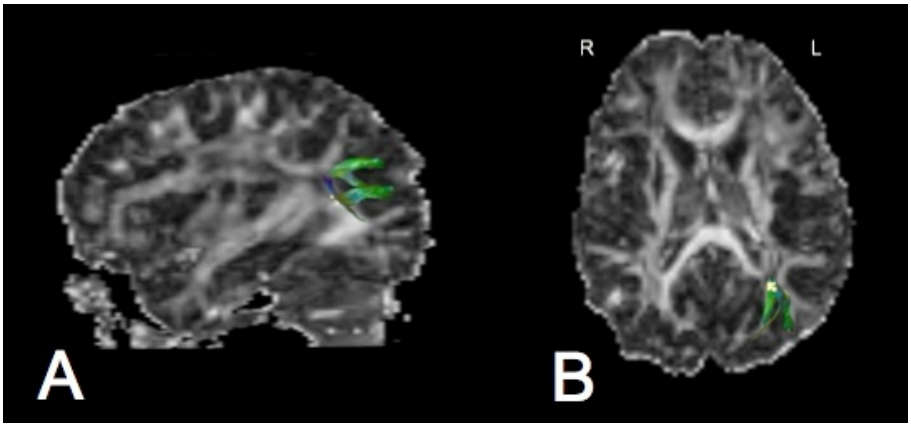

Figure 28. Fibertract of region in occipital lobe.

Slice 29

Two regions correlating FA with WRAT-M were found in this particular slice (Figure 29). These regions include a frontal and an occipital location (Figure 30).

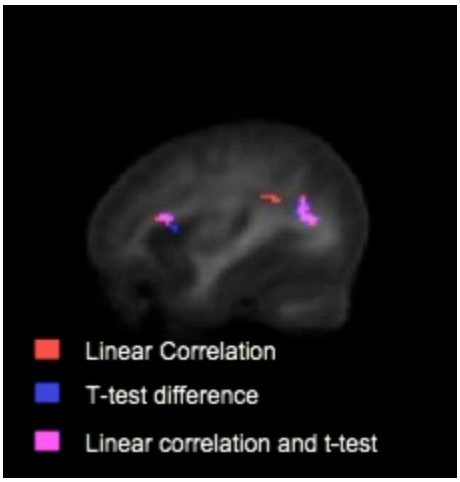

Figure 29. Regions in which FA was correlated with WRAT-M (red) and regions found to have a significant difference between control and MD groups (blue). Pink voxels display overlap between the two analyses. The red parietal region was disregarded due to low FA values (FA < 0.2).

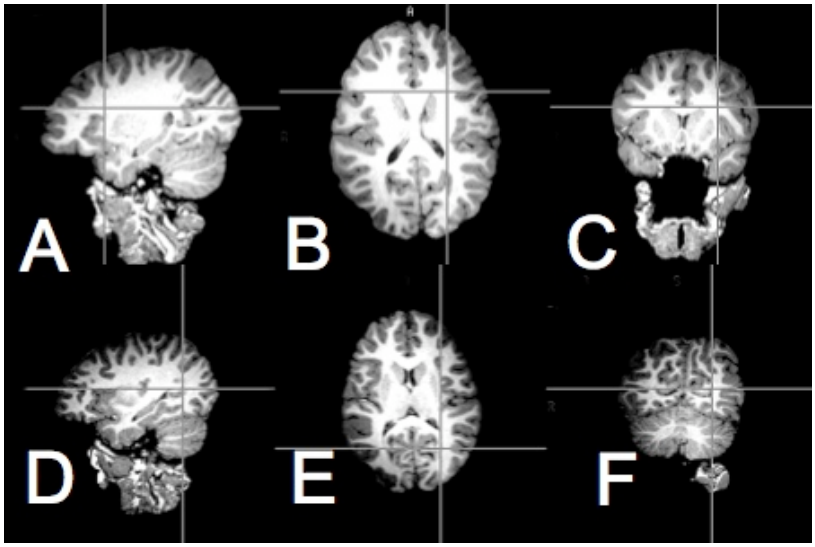

Figure 30. Anatomical locations of regions correlated with WRAT-M. (a),(b), and (c) show the sagittal, axial, and coronal views, respectively, of the frontal region, while (d),(e), and (f) show the location of the occipital region.

This particular slice also displayed a relationship between FA values and the WRAT-R exam (Figure 31). One of these regions overlapped with the frontal region found in the math correlation, while two other regions were found in the pre-frontal portion of the brain.

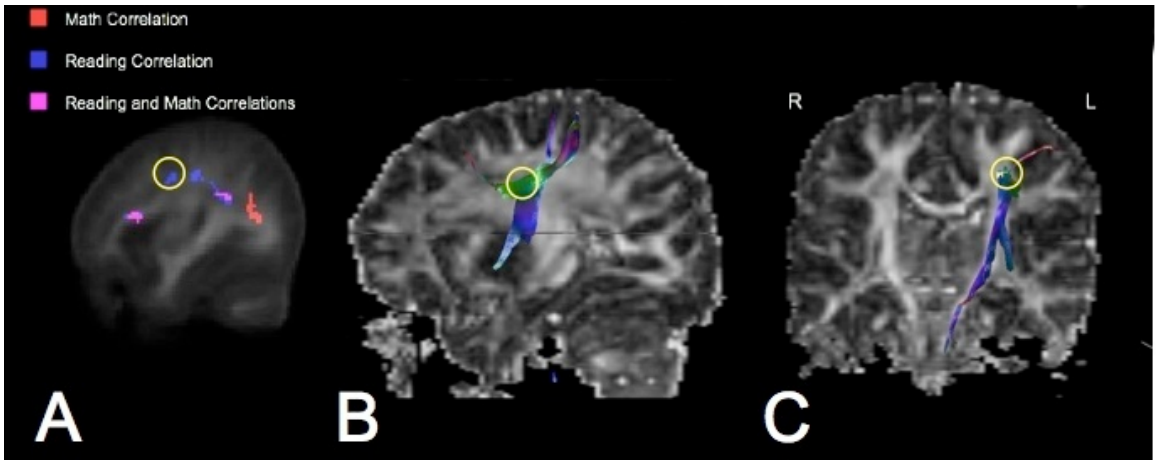

Figure 31. (a) Regions in which FA was correlated with WRAT-M (red), and WRAT-R (blue). Pink voxels display overlap between the two regions. (b) Sagittal and (c) coronal views of the fibertract using the seedpoint from the circled reading region in (a).

Slice 30

Slice 30 displayed regions that correlated with both WRAT-M and WRAT-R (Figure 32). A frontal region shows overlap between regions that correlate with both WRAT-M and WRAT-R. A prefrontal region is found that correlates with WRAT-R only.

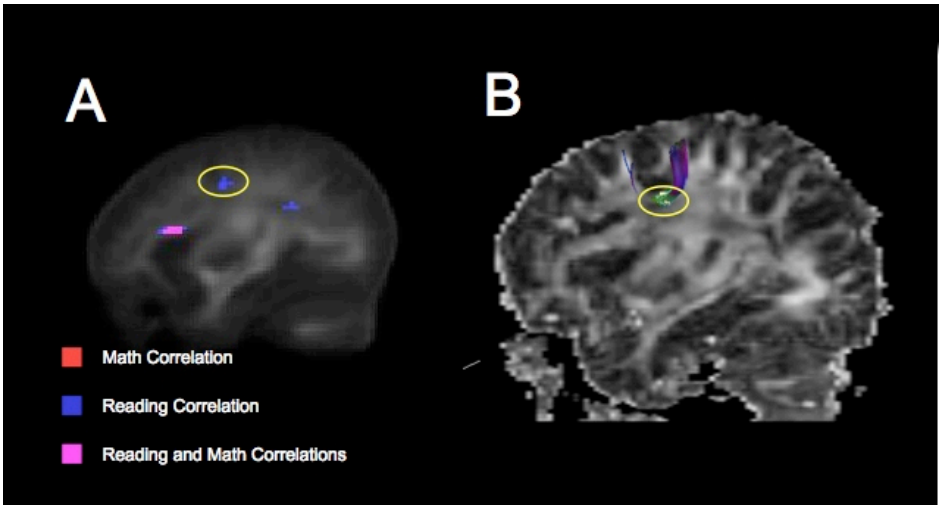

Figure 32. (a) Regions correlated with WRAT-M (red), and WRAT-R (blue) in slice 30. Pink voxels display overlay between the two regions. (b) Sagittal view of the fibertract using the seedpoint from the circled reading region in (a).

Frontal Region - Slices 27-31

The frontal ROI in which FA was shown to correlate with both WRAT-M and WRAT-R is a large region that spans over five sagittal slices (Figure 33). The two leftmost slices (27,28) show this frontal region is correlated to only the WRAT-M test, while the others (29-31) show the region correlates with both scores. Fibertracking of this region shows that this is local fibertract, possibly terminated medially by partial volume averaging (Figure 34).

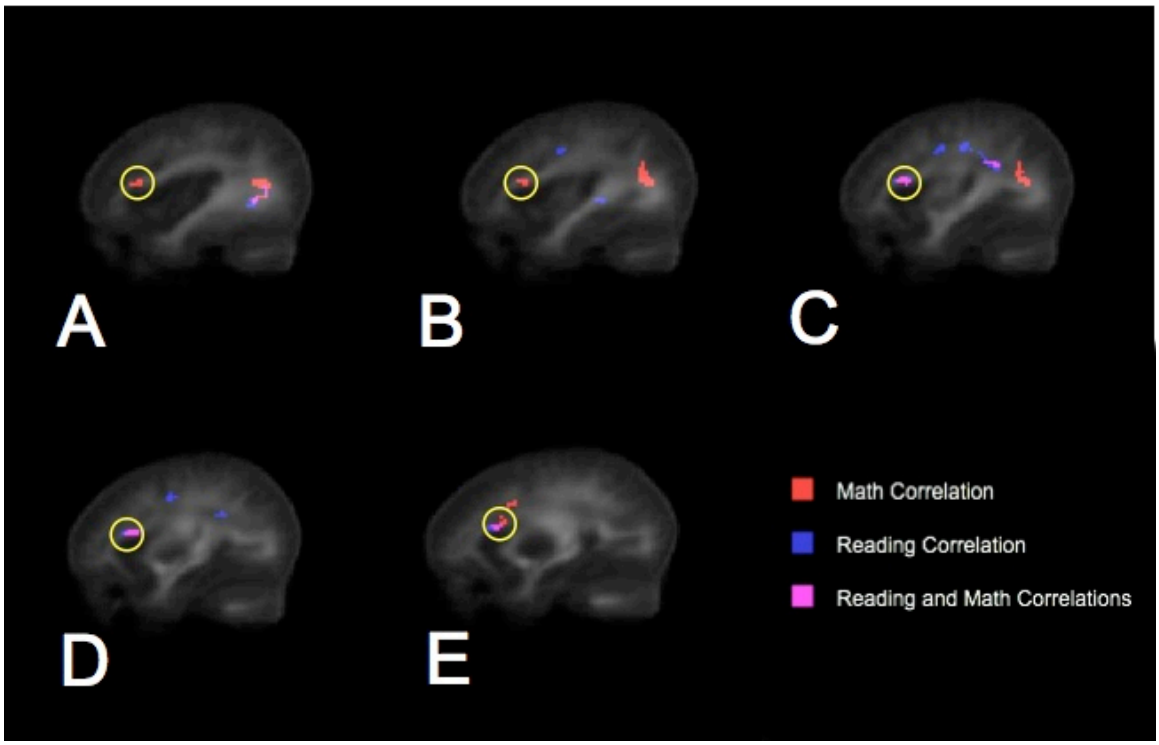

Figure 33. (a-e) Sagittal views of continuous slices with frontal ROI circled. Red voxels show correlation with WRAT-M, blue voxels show correlation with WRAT-R, and pink voxels show overlap.

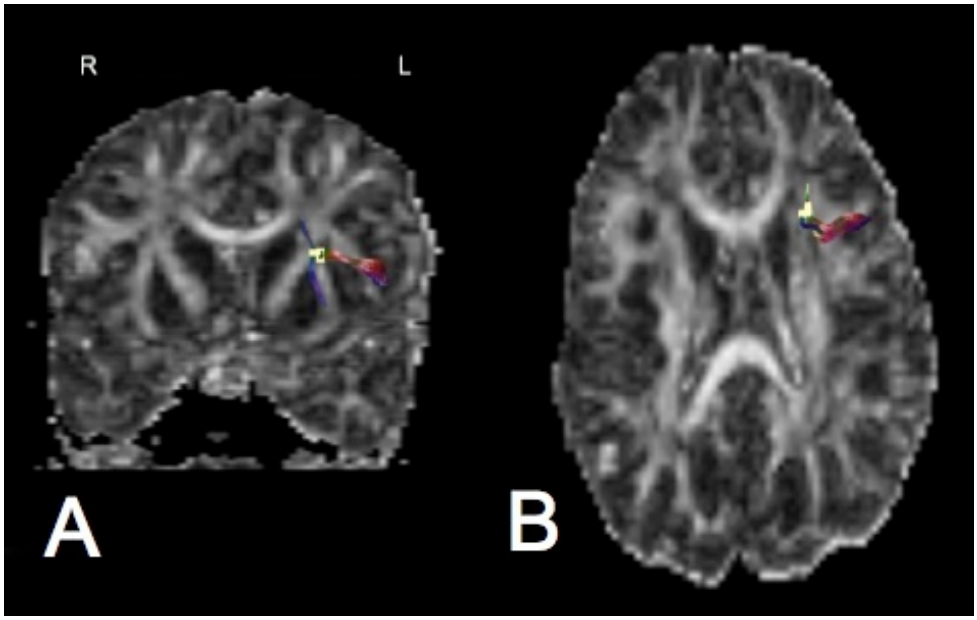

Figure 34. (a) Coronal and (b) axial view of fibertract of frontal regions found in slices 27-31.

Math Region Correlations Between FA and In-Magnet Math Tasks

Several of these math regions were found to correlate with in-magnet math task performance. Table 3 shows the correlation of the region found in the parietal area of slice 24, the occipital slices in 26-28, and the frontal regions in slices 27-31 (Table 3).

Table 3. Correlation of FA in ROI with in-magnet task performance. Note: A=Approximation, PR=Procedural, EC=Exact Calculation, PJ=Proximal Judgment, RT=Reaction Time, PC=Percent Correct. See Figure 15 for details.

FA REGION		A RT	A PC	PR RT	PR PC	EC RT	EC PC	PJ RT	PJ PC	WRAT-M	WRAT-R
Parietal 24	Pearson Correlation	-0.07	.583**	-0.04	.511**	-0.096	.634**	0.108	.487**	.570**	.426*
	Sig. (2-tailed)	0.73	0.00	0.84	0.01	0.63	0.00	0.58	0.01	0.00	0.02
Occipital 26	Pearson Correlation	-0.024	.629**	-0.04	.764**	-0.195	.583**	0.023	.714**	.594**	.555**
	Sig. (2-tailed)	0.91	0.00	0.84	0.00	0.32	0.00	0.91	0.00	0.00	0.00
	N	27	28	27	26	28	28	28	28	28	28
Occipital 27	Pearson Correlation	0.004	.659**	-0.084	.637**	-0.232	.490**	0.081	.565**	.519**	.481**
	Sig. (2-tailed)	0.99	0.00	0.68	0.00	0.24	0.01	0.68	0.00	0.01	0.01
	N	27	28	27	26	28	28	28	28	28	28
Occipital 28	Pearson Correlation	-0.108	.497**	-0.09	.463*	-0.327	.452*	-0.115	.424*	.534**	.417*
	Sig. (2-tailed)	0.59	0.01	0.66	0.02	0.09	0.02	0.56	0.02	0.00	0.03
	N	27	28	27	26	28	28	28	28	28	28
Frontal 28	Pearson Correlation	0.04	.564**	0.061	.718**	-0.119	.632**	0.083	.509**	.588**	.543**
	Sig. (2-tailed)	0.84	0.00	0.76	0.00	0.55	0.00	0.68	0.01	0.00	0.00
	N	27	28	27	26	28	28	28	28	28	28
Frontal 29	Pearson Correlation	0.162	.605**	0.025	.711**	-0.205	.616**	0.012	.543**	.592**	.677**
	Sig. (2-tailed)	0.42	0.00	0.90	0.00	0.30	0.00	0.95	0.00	0.00	0.00
	N	27	28	27	26	28	28	28	28	28	28
Frontal 30	Pearson Correlation	0.216	.498**	0.021	.598**	-0.275	.493**	-0.119	.428*	.528**	.702**
	Sig. (2-tailed)	0.28	0.01	0.92	0.00	0.16	0.01	0.55	0.02	0.00	0.00
	N	27	28	27	26	28	28	28	28	28	28
Frontal 31	Pearson Correlation	-0.062	.507**	-0.012	.539**	-0.252	.486**	-0.217	0.347	.524**	.566**
	Sig. (2-tailed)	0.76	0.01	0.95	0.00	0.20	0.01	0.27	0.07	0.00	0.00
	N	27	28	27	26	28	28	28	28	28	28
**	Correlation is significant at the 0.01 level (2-tailed).										
*	Correlation is significant at the 0.05 level (2-tailed).										

Reading Region

An additional reading region was found in the left hemisphere (Figure 35).This region is the most medial found and is connected to the corpus callosum.

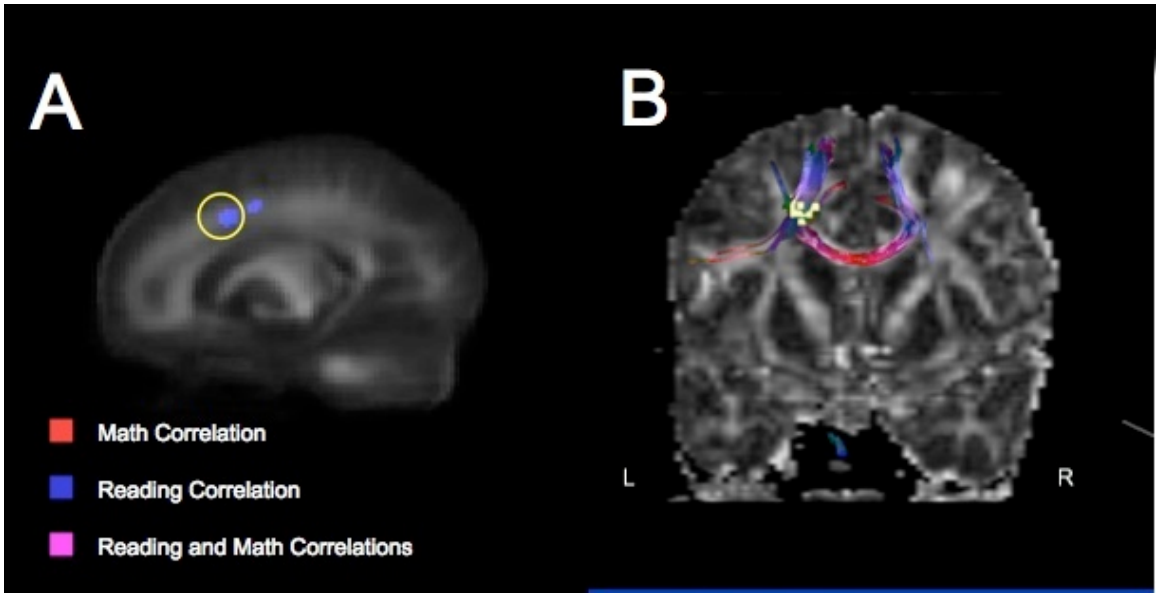

Figure 35 (a) Additional region to correlate with WRAT-R scores. (b) Fibertract of circled region in (a).

Correlations with fMRI

One region was found to correlate with fMRI activation (Figure . This region was found in the left parietal cortex during the procedural in-magnet math task. This is very similar to the region found to correlate with WRAT-M in slice 24. Fibertracts were found that cross both regions, and extend to the left parietal cortex, where the fMRI activation occurred.

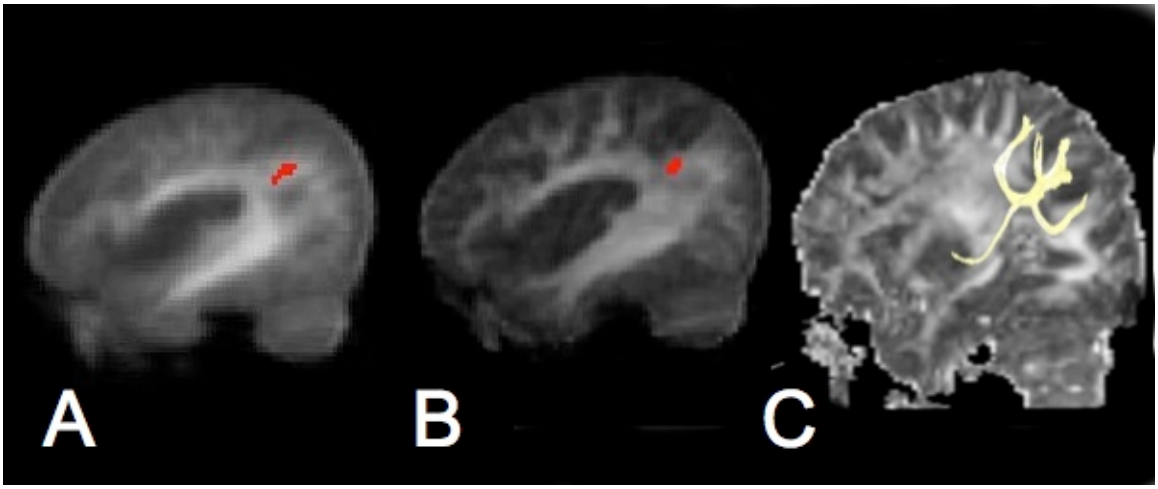

Figure 36. Correlation with fMRI. (a) Left parietal ROI in which FA correlated with WRAT-M score. (b) Left parietal ROI correlating with fMRI activation during the procedural in-magnet task. (c) Fibertract that enters both regions found in (a) and (b).

CHAPTER IV

DISCUSSION

This study found many regions in the white matter in which children with average math ability had a higher FA scores than those with math difficulty. In most of these regions FA was correlated with math ability in the entire study population. The largest regions were found in the left hemisphere, mainly in the parietal and occipital regions. These cortical areas had been previously linked to functional activation during mental math calculations, including the HIPS and posterior superior parietal lobe. Fibertracking of these regions found tracts that terminate in the cortex of the parietal and occipital lobes, maintaining the possibility that there is communication between the two cortical areas during certain math tasks. (Figure . Each of these regions was significantly correlated with performance in all of the math tasks, however there was no correlation between FA and reaction time.

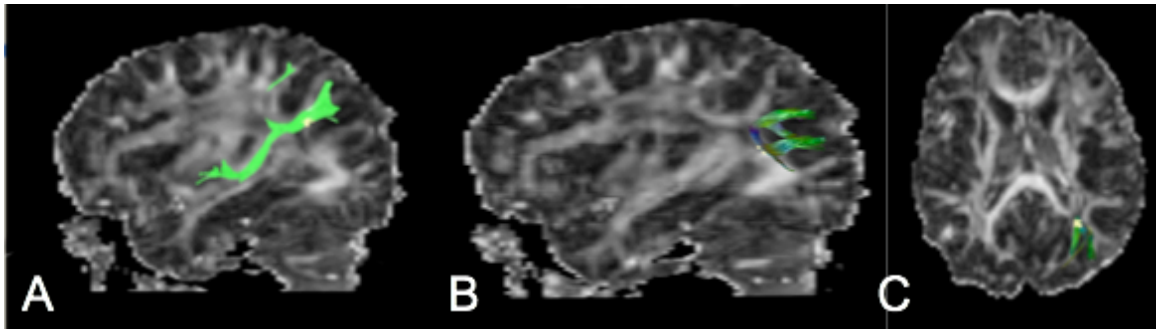

Figure 37. Parietal and occipital fibertracts. (a) Parietal tract. (b) and (c) Occipital tract in sagittal and axial views.

Using fMRI activation measures, it was found that there is a correlation in the left parietal lobe between FA and functional activation during a proximal judgment task. This cortical activation was also found in the left parietal lobe in the proximal judgment task, suggesting that the fMRI region supplies axons to the white matter region where the correlation is seen. This confirms previous studies linking math ability and the left parietal lobe, as well as our hypothesis of a link between functional activation and white matter integrity in children with math difficulties.

There was also a large region in the frontal lobe in which FA was correlated with math ability, with most of the region also correlating with in-magnet task performance. This is an unexpected result as it was hypothesized that there would only be correlation in the parietal and occipital regions. Further analysis showed that these same frontal regions are also correlated with reading ability, suggesting that there is a relationship in the white matter tracts between reading procedures and math calculations. This frontal region could provide a passage way connecting math areas in the parietal lobe with regions in the frontal lobe in order to access working memory needed in math computations.

In addition to the regions correlated with math ability, there were many regions found in the white matter that correlated with reading ability only. Tractography confirms these lie in the superior longitudinal fasciculus (SLF), corona radiata, and corpus callosum. This is encouraging because previous studies suggest these fibers are highly likely to be involved in reading (Figure 38).

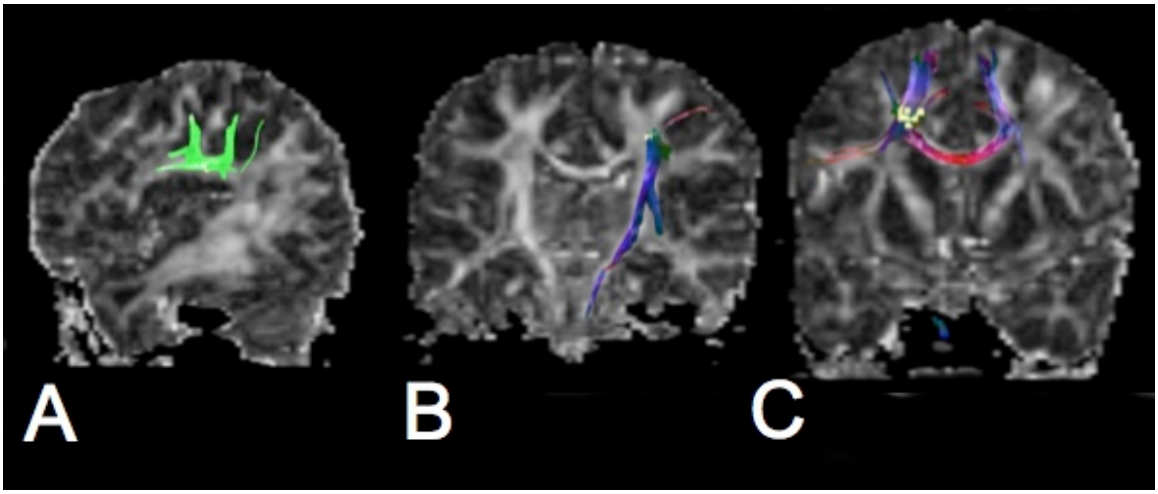

Figure 38. Fibertracts of regions correlated with reading ability found in current study. (a) Region (yellow) in SLF. (b) Region (yellow) in corona radiata. (c) Region (yellow) found in anterior corpus callosum. These are similar to the regions in Figure 14.

Although both reading and math computations involved a complex system of cortical and white matter networks, there is evidence that they use independent white matter bundles in certain occasions and share common bundles in others. This study found that math computation is highly related to white matter integrity in the left parietal and occipital regions of the brain, whereas reading is correlated with white matter FA in the SLF, corpus callosum, and corona radiata. Math and reading share a white matter tract in the frontal lobe. In order to understand the underlying problem in learning disabilities such as these, it is necessary to find how these two complex cognitive functions relate to one another, both in white matter structure and in cortical activation.

There are many questions that need to be answered regarding white matter tractography, reading, and math ability. The largest question is if this evidence is correct and if so, whether the white matter deficit can this be reversed. Is there an intervention method that can repair neural networks so they function as well as in a child with average

ability? At what age should intervention take place? Although intervention is critical in advancing the skills of the child, especially those with difficulties, there is much skepticism that this intervention will change or repair neural networks.

Regions in which FA was negatively correlated with math ability were not studied, although there is evidence that these regions exist in a limited number of white matter tracts. These regions may give some insight into how children with math difficulties have adapted to having limited FA in key math regions. These brains may have created alternative routes for cortical processing during math computations, which may result in difficulties in math computations. If indeed there are such regions, where do they lead? What cortical activation is alternatively taking place such that white matter tracts are 'recruited' in children with math difficulties? Children with math difficulties must utilize an alternative neural network, but it remains to be seen exactly what network and to what extent it is utilized.

Future Aims

This study has given insight into the neural processes engaged during math computation, however it also provides many more questions requiring answers. Certainly a high priority is to incorporate more children into the study, especially children predisposed to math difficulty in order to answer these questions. The first aim is to work with fMRI results and determine the relationship between the DTI results and the cortical activations seen in functional imaging.

The second aim is to determine the relationship between intervention and white matter integrity. It has been proposed that a cohort of children with math difficulties be

imaged pre-intervention and then imaged again after a period of intense math intervention. These data will be analyzed to determine if there is a physical difference in the white matter makeup between the pre-intervention scan and the post-intervention scan.

A third aim is to find regions in the white matter that show a negative correlation with FA, or regions in which children with math difficulties show a higher FA than the controls. This will provide information as to how children with math difficulties utilize alternative networks during math computation. Along the same lines, it would be necessary to determine if there are higher functional activations during certain tasks in children with math difficulties by using fMRI. These two imaging datasets can be combined to determine a relationship between cortical functioning and white matter microstructure.

CHAPTER V

CONCLUSIONS

The results found in this study suggest there are regions in the brain in which white matter integrity is compromised in children with math difficulties. This was found by correlating FA values with math ability. If these deficits in white matter can be found early in a child's life, it may be possible to provide intervention, change the developmental trajectory of white matter pathways, and enable the white matter to become more like that in children with average math ability. Several regions were also correlated with reading ability, mainly in the left SLF, coronal radiata, and anterior corpus callosum. These findings were independent of math ability, although an underlying relationship has yet to be investigated. Future work will investigate the relationship between reading and math ability and how their respective cortical processing utilizes white matter tracts.

APPENDIX A

SAMPLE CONFIGURATION FILE FOR RIGID REGISTRATION

[Number of image pairs (default: the number of reference images)]
1

[*File name of the reference image]
/home/lorangct/craig/DTI_Rotate/Math_102_epiT2.img

[*File name of the target image]
/home/lorangct/craig/3D_Scans/Math_102_3D.REC

[File name of the input transformation]

[Format of the input transformation: 1-parameters 2-deformation field 3-initial position (default: 1)]

[File name of the reference registered to the target]
/home/lorangct/craig/DTI_Rigid_Registration/Trial_2/Math_102_3D_reg.REC

[File name of the target registered to the reference]

[File name of the output transformation from the reference to the target]
/home/lorangct/craig/DTI_Rigid_Registration/Trial_2/Math_102_3D_reg.mat

[File name of the output transformation from the target to the reference]

[Format of the output transformation file: 1-parameter file 2-deformation field file (default: 1)]

[*Dimensions of the reference image]
128 128 60

[*Dimensions of the target image]
256 256 170

[*Voxel sizes of the reference image in millimeters]
2 2 2

[*Voxel sizes of the target image in millimeters]
1 1 1

[Orientation of the reference image in LRPASI (default: 2 -3 -1)]
1 2 3

[Orientation of the target image in LRPASI (default: 2 -3 -1)]

[Header size of the reference image in bytes (default: 0)]

[Header size of the target image in bytes (default: 0)]

[Data type of the reference image: 1-uint8; 2-int16; 4-int32; 6-float; 7-double (default: 2)]

[Data type of the target image: 1-uint8; 2-int16; 4-int32; 6-float; 7-double (default: 2)]

[Byte order of the reference image: 0-big endian(Sun); 1-little endian(Intel) (default: 0)]
1

[Byte order of the target image: 0-big endian(Sun); 1-little endian(Intel) (default: 0)]
1

[Intensity window of the histogram of the reference image (default: min() max())]
0 500

[Intensity window of the histogram of the target image (default: min() max())]
0 300

[Intensity range of the background of the reference image (default: 0 0)]

[Intensity range of the background of the target image (default: 0 0)]

[ROI in the target image (default: 0 dx-1 0 dy-1 0 dz-1, given the dimensions are dx dy dz)]

[Sampling intervals of the target image (default: 1 1 1)]

[Reformat the target image before registration: 0-Auto; 1-Yes; 2-No (default: 0)]

[Smooth the images before registration: 1-Yes; 2-No (default: 1)]

[Number of bins in the reference and target image histograms (default: 64 64)]

[Type of interpolation used in the reference image: 1-trilinear; 2-partial volume (default: 2)]

[Optimization order (default: 1 2 4 5 6 3 0 0 0 0 0 0)]

[Step sizes of optimization (default: 1 1 1 1 1 1 .1 .1 .1 .1 .1 .1)]

[Powell parameters: pfTol pMaxIter bxTol bMaxIter (default: 1e-3 100 2e-4 200)]

[Number of resolution levels (default: 2)]

[Registration criterion: 0-MI; 1-NMI (default: 0)]
1

[Initial position: (default: 0 0 0 0 0 0 1 1 1 0 0 0)]

[File name of the input evaluation points]

[File name of the output evaluation points]

[Mapping direction of the evaluation points: 0-reference=>target; 1-target=>reference (default: 1)]

[Unit of the evaluation points: 0-pixel; 1-millimeter (default: 0)]

APPENDIX B

SAMPLE CONFIGURATION FILE FOR NON-RIGID REGISTRATION

```
SOURCE:
c:\src1.vol
c:\src2.vol
0

TARGET:
c:\trg1.vol
c:\trg2.vol
0

256
256
198
1
1

PARAMETERS:
15
2
2
3 4 5 6 7 8 9 10 12 16 20 26 32 40 50
3 4 5 6 7 8 9 10 12 16 20 26 32 40 50
6 32
0 127
0 127
32
32
0.3

CONFIGURATION:
1
0
1.6
0.0001
0.0005
0.01
0.1
```

0.0001
1 1 1
1

OUTPUT:
c:\src1_to_trg1.vol
c:\src2_to_trg2.vol

OUTPUT:
c:\trg1_to_src1.vol
c:\trg2_to_src2.vol

REFERENCES

Alexander, A. L., J. E. Lee, M. Lazar, and A. S. Field. 2007. Diffusion tensor imaging of the brain. *Neurotherapeutics* 4 (3):316-29.

Bammer, R. 2003. Basic principles of diffusion-weighted imaging. *Eur J Radiol* 45 (3):169-84.

Basser PJ, Mattiello J, LeBihan D. 1994. MR Diffusion in Tensor Spectroscopy and Imaging. *Biophysics Journal* 66 (1):259-267.

Beaulieu, C. 2002. The basis of anisotropic water diffusion in the nervous system - a technical review. *Nmr in Biomedicine* 15 (7-8):435-455.

Beaulieu, C., C. Plewes, L. A. Paulson, D. Roy, L. Snook, L. Concha, and L. Phillips. 2005. Imaging brain connectivity in children with diverse reading ability. *Neuroimage* 25 (4):1266-71.

Ben-Shachar, M., R. F. Dougherty, and B. A. Wandell. 2007. White matter pathways in reading. *Current Opinion in Neurobiology* 17 (2):258-270.

Chochon, F., L. Cohen, P. F. van de Moortele, and S. Dehaene. 1999. Differential contributions of the left and right inferior parietal lobules to number processing. *J Cogn Neurosci* 11 (6):617-30.

Cohen, L., S. Dehaene, F. Chochon, S. Lehericy, and L. Naccache. 2000. Language and calculation within the parietal lobe: a combined cognitive, anatomical and fMRI study. *Neuropsychologia* 38 (10):1426-40.

Corbetta, M., J. M. Kincade, J. M. Ollinger, M. P. McAvoy, and G. L. Shulman. 2000. Voluntary orienting is dissociated from target detection in human posterior parietal cortex. *Nat Neurosci* 3 (3):292-7.

Dehaene, S., G. Dehaene-Lambertz, and L. Cohen. 1998. Abstract representations of numbers in the animal and human brain. *Trends Neurosci* 21 (8):355-61.

Dehaene, S., M. Piazza, P. Pinel, and L. Cohen. 2003. Three Parietal Circuits for Number Processing. *Cognitive Neuropsychology* 20 (3):487-506.

Dehaene, S., E. Spelke, P. Pinel, R. Stanescu, and S. Tsivkin. 1999. Sources of mathematical thinking: behavioral and brain-imaging evidence. *Science* 284 (5416):970-4.

Gary Wilkenson, PhD. 1993. Wide Range Achievement Test - Third Edition (WRAT-3): Wide Range, Inc.

Geary, DC. 2004. Mathematics and Learning Disabilities. *Jornal of Learning Disabilities* 37 (1):4-15.

Hasan, K. M., D. L. Parker, and A. L. Alexander. 2001. Comparison of gradient encoding schemes for diffusion-tensor MRI. *J Magn Reson Imaging* 13 (5):769-80.

Hill, H., M. W. O'Boyle, and J. Hathaway. 1998. Cortical Distribtution of Neural Activity for Component Processes in Mental Rotation. *Cortex* 34:707-718.

Horwitz, B., J. M. Rumsey, and B. C. Donohue. 1998. Functional connectivity of the angular gyrus in normal reading and dyslexia. *Proc Natl Acad Sci U S A* 95 (15):8939-44.

Jellison, B. J., A. S. Field, J. Medow, M. Lazar, M. S. Salamat, and A. L. Alexander. 2004. Diffusion tensor imaging of cerebral white matter: a pictorial review of physics, fiber tract anatomy, and tumor imaging patterns. *AJNR Am J Neuroradiol* 25 (3):356-69.

Jezzard, P., A. S. Barnett, and C. Pierpaoli. 1998. Characterization of and correction for eddy current artifacts in echo planar diffusion imaging. *Magn Reson Med* 39 (5):801-12.

Kaufmann, L., P. Handl, and B. Thony. 2003. Evaluation of a numeracy intervention program focusing on basic numerical knowledge and conceptual knowledge: a pilot study. *J Learn Disabil* 36 (6):564-73.

Klingberg, T., M. Hedehus, E. Temple, T. Salz, J. D. Gabrieli, M. E. Moseley, and R. A. Poldrack. 2000. Microstructure of temporo-parietal white matter as a basis for reading ability: evidence from diffusion tensor magnetic resonance imaging. *Neuron* 25 (2):493-500.

Le Bihan, D. 1991. Molecular diffusion nuclear magnetic resonance imaging. *Magn Reson Imaging* 7:1-30.

Le Bihan, D., J. F. Mangin, C. Poupon, C. A. Clark, S. Pappata, N. Molko, and H. Chabriat. 2001. Diffusion tensor imaging: Concepts and applications. *Journal of Magnetic Resonance Imaging* 13 (4):534-546.

Le Bihan, D., C. Poupon, A. Amadon, and F. Lethimonnier. 2006. Artifacts and pitfalls in diffusion MRI. *J Magn Reson Imaging* 24 (3):478-88.

Lee, K. M. 2000. Cortical areas differentially involved in multiplication and subtraction: a functional magnetic resonance imaging study and correlation with a case of selective acalculia. *Ann Neurol* 48 (4):657-61.

Li, R. 2001. EECS, Vanderbilt University, Nashville.

Maes, F., A. Collignon, D. Vandermeulen, G. Marchal, and P. Suetens. 1997. Multimodality image registration by maximization of mutual information. *IEEE Trans Med Imaging* 16 (2):187-98.

Matthews, P. M., and P. Jezzard. 2004. Functional magnetic resonance imaging. *J Neurol Neurosurg Psychiatry* 75 (1):6-12.

Niogi, S. N., and B. D. McCandliss. 2006. Left lateralized white matter microstructure accounts for individual differences in reading ability and disability. *Neuropsychologia* 44 (11):2178-88.

O'Boyle, M. W., R. Cunnington, T. J. Silk, D. Vaughan, G. Jackson, A. Syngeniotis, and G. F. Egan. 2005. Mathematically gifted male adolescents activate a unique brain network during mental rotation. *Brain Res Cogn Brain Res* 25 (2):583-7.

Papadakis, N. G., C. D. Murrills, L. D. Hall, C. L. Huang, and T. Adrian Carpenter. 2000. Minimal gradient encoding for robust estimation of diffusion anisotropy. *Magn Reson Imaging* 18 (6):671-9.

Pesenti, M., M. Thioux, X. Seron, and A. De Volder. 2000. Neuroanatomical substrates of arabic number processing, numerical comparison, and simple addition: a PET study. *J Cogn Neurosci* 12 (3):461-79.

Piazza, M., A. Mechelli, B. Butterworth, and C. J. Price. 2002. Are subitizing and counting implemented as separate or functionally overlapping processes? *Neuroimage* 15 (2):435-46.

Pierpaoli, C., and P. J. Basser. 1996. Toward a quantitative assessment of diffusion anisotropy. *Magn Reson Med* 36 (6):893-906.

Pierpaoli, C., P. Jezzard, P. J. Basser, A. Barnett, and G. Di Chiro. 1996. Diffusion tensor MR imaging of the human brain. *Radiology* 201 (3):637-48.

Pinel, P., S. Dehaene, D. Riviere, and D. LeBihan. 2001. Modulation of parietal activation by semantic distance in a number comparison task. *Neuroimage* 14 (5):1013-26.

Robichon, F., and M. Habib. 1998. Abnormal callosal morphology in male adult dyslexics: relationships to handedness and phonological abilities. *Brain Lang* 62 (1):127-46.

Rohde, G. K., A. Aldroubi, and B. M. Dawant. 2003. The adaptive bases algorithm for intensity-based nonrigid image registration. *IEEE Trans Med Imaging* 22 (11):1470-9.

Rorden, C., and M. Brett. 2000. Stereotaxic display of brain lesions. *Behav Neurol* 12 (4):191-200.

Rumsey, J. M., M. Casanova, G. B. Mannheim, N. Patronas, N. De Vaughn, S. D. Hamburger, and T. Aquino. 1996. Corpus callosum morphology, as measured with MRI, in dyslexic men. *Biol Psychiatry* 39 (9):769-75.

Shalev, R. S. 2004. Developmental dyscalculia. *J Child Neurol* 19 (10):765-71.

Smith, S. M. 2002. Fast robust automated brain extraction. *Hum Brain Mapp* 17 (3):143-55.

Spelke, E., and S. Dehaene. 1999. Biological foundations of numerical thinkingResponse to T.J. Simon (1999). *Trends Cogn Sci* 3 (10):365-366.

Stejskal, E. O., and J. E. Tanner. 1965. SPIN DIFFUSION MEASUREMENTS - SPIN ECHOES IN PRESENCE OF A TIME-DEPENDENT FIELD GRADIENT. *Journal of Chemical Physics* 42 (1):288-&.